Structural Dynamics of Spin Crossover in Iron(II) Complexes with Extended-Tripod Ligands

Philipp Stock [1], Dennis Wiedemann [1] (iD), Holm Petzold [2] and Gerald Hörner [1,*]

[1] Institut für Chemie, Technische Universität Berlin, Straße des 17. Juni 135, 10623 Berlin, Germany; philippstock@yahoo.de (P.S.); dennis.wiedemann@chem.tu-berlin.de (D.W.)
[2] TU Chemnitz, Institut für Chemie, Anorganische Chemie, Straße der Nationen 62, 09111 Chemnitz, Germany; holm.petzold@chemie.tu-chemnitz.de
* Correspondence: gerald.hoerner@tu-berlin.de; Tel.: +49-30-314-27936
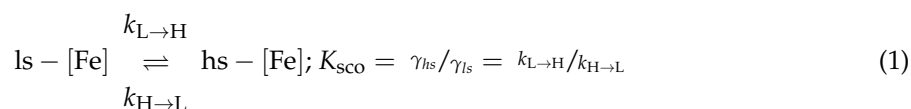
Abstract: Selective manipulation of spin states in iron(II) complexes by thermal or photonic energy is a desirable goal in the context of developing molecular functional materials. As dynamic spin-state equilibration in isolated iron(II) complexes typically limits the lifetime of a given spin state to nanoseconds, synthetic strategies need to be developed that aim at inhibited relaxation. Herein we show that modulation of the reaction coordinate through careful selection of the ligand can indeed massively slow down dynamic exchange. Detailed structural analysis of **[FeL]$^{2+}$** and **[ZnL]$^{2+}$** (**L**: tris(1-methyl-2-{[pyridin-2-yl]-methylene}hydrazinyl)phosphane sulfide) with crystallographic and computational methods clearly reveals a unique trigonal-directing effect of the extended-tripod ligand **L** during spin crossover, which superimposes the ubiquitous [FeN$_6$] breathing with trigonal torsion, akin to the archetypal Bailar twist. As a consequence of the diverging reaction coordinates in **[FeL]$^{2+}$** and in the **tren**-derived complex **[Fe(tren)py$_3$]$^{2+}$**, their thermal barriers differ massively, although the spin crossover energies are close to identical. As is shown by time-resolved transient spectroscopy and dynamic ^{1}H-NMR line broadening, reference systems deriving from **tren** (tris-(2-aminoethyl)amine), which greatly lack such trigonal torsion, harbor very rapid spin-state exchange.

Keywords: spin crossover; Bailar twist; prismatic coordination; line broadening; chemical exchange

1. Introduction

Numerous first-row transition metal complexes with a d^4 to d^7 electron configuration possess energetically close lying spin states. A jump in thermal energy or admittance of alternative energy sources (X-rays, UV/Vis photons) can be used to stimulate crossover among these states (spin crossover, SCO) [1–5]. The spin isomers are sharply discretized by their magnetic properties, but in many cases they also differ substantially in complementary observables, such as UV/Vis absorption. It is the combined switching of magnetic and optical properties that renders this class of compounds highly promising as opto-magnetic actors and sensors [6,7]. The most prominent example is SCO between the low-spin (**ls**; $^1A_{1g}/t_{2g}^6$, $S = 0$) and high-spin (**hs**; $^5T_{2g}/t_{2g}^4e_g^2$, $S = 2$) states in iron(II) complexes (d^6) (Equation (1); γ_{hs} and γ_{ls} denote the spin-state molar fractions).

$$\text{ls} - [\text{Fe}] \underset{k_{\text{H}\to\text{L}}}{\overset{k_{\text{L}\to\text{H}}}{\rightleftharpoons}} \text{hs} - [\text{Fe}]; \; K_{\text{sco}} = \gamma_{hs}/\gamma_{ls} = k_{\text{L}\to\text{H}}/k_{\text{H}\to\text{L}} \tag{1}$$

As a prototypical example of a chemical equilibrium, the spin states underlie constant exchange with $k_{\text{H}\to\text{L}}$ and $k_{\text{L}\to\text{H}}$ as the rate constants of **hs** and **ls** decay, respectively. Thermal equilibration can be sometimes "frozen out" at cryogenic temperatures [8–12], so that minority states can be enriched as

meta-stable species through irradiation with light or via rapid freezing. The former effect was coined as light-induced excited spin-state trapping, LIESST, whereas thermal induced excited spin-state trapping, TIESST, has been established as an alternative method for kinetic stabilization via rapid freezing [9]. Around ambient temperature, however, the exchange reactions are very rapid, leading to randomizing spin states within a few nanoseconds in most iron(II) complexes [13–24].

Our serendipitous observation of spin state lifetimes in the microsecond range for a number of six-coordinate iron(II) complexes therefore marks a notable exception that demands rationalization [25,26]. Ligands of the extended-tripod type with a unique thiophosphoryl capping unit (**L** in Scheme 1 and derivatives thereof) were found to harbor hindered SCO kinetics, irrespective of solvent nature and the presence of dioxygen. Through synthetic fine tuning of the ligand periphery and of the heterocycle, we could recently further extend the time domain of SCO to the millisecond range [27]. Based on extended laser-flash photolysis (LFP) studies in concert with XRD-calibrated density-functional theory modeling, we correlated the exceptionally slow SCO kinetics with the nature of SCO reaction coordinates.

In this picture, slow exchange prevails, when the reaction coordinate consists of two components; (i) trivial isotropic "breathing" of the coordination sphere due to (de)population of anti-bonding e_g-type orbitals in the (**ls**) **hs** state; (ii) anisotropic torsion of the coordination sphere along a (pseudo) C_3 axis, akin to Bailar's trigonal twist [28]. Actually, **L** and derived ligands are known to facilitate the synthesis of trigonal prismatic complexes [29–31]. This correlation acknowledges previous structure-spin state correlations [32], that are based on structural–chemical considerations going back to the early 1970s [33–42]. In particular, the idea of a taming of the SCO dynamics via ligand-imposed trigonal torsion is a recurrent motif of research. The antipode of fast exchange prevails, as long as the reaction coordinate is largely limited to isotropic "breathing". Intriguingly, the topologically related family of iron(II) complexes with **tren**-derived ligands (**tren**: tris-(2-aminoethyl)amine) falls in this second class of rapidly exchanging SCO systems. Large room temperature exchange rate constants k_{obs} of 1.1×10^7 s^{-1} and 1.4×10^7 s^{-1} have been extracted from LFP studies of **[Fe(tren)py₃]**(ClO$_4$)$_2$ and **[Fe(tren)imid₃]**(BF$_4$)$_2$, respectively [27,43].
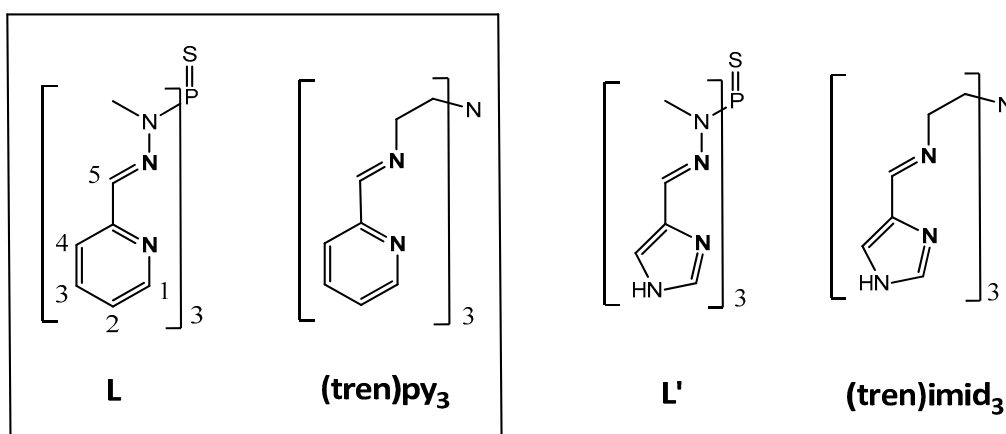
Scheme 1. Extended tripodal $\kappa^6 N$ polyimine ligands investigated in this study (proton numbering in **L** applies also for **(tren)py₃**); iron(II) complexes of the literature known imidazole ligands **L'** [31] and **(tren)imid₃** [44–48] serve as DFT reference systems.

As a matter of fact, high susceptibility towards even subtle variations in the ligand sphere is a more general feature of the SCO phenomenon. Structure–function relations have been discussed in some detail [49], mainly with respect to SCO thermodynamics and control of cooperativity among SCO manifolds [50], however. By contrast, the probably broadest experimental work on SCO dynamics dates back to 1996 [22], while the latest review in the field stems from 2004 [21]. Clearly, the knowledge on the SCO exchange kinetics in general and the ligand-borne effects on kinetics in particular require

significant extension. In this work we therefore set out to provide deeper insights into the structural dynamics of spin crossover of the complexes **[FeL]$^{2+}$** and **[Fe(tren)py$_3$]$^{2+}$** and its interrelations with the phenomenological spin-state dynamics. X-ray crystallography of zinc(II) and iron(II) complexes of **L** and comparison with **[FeL']$^{2+}$** [27] served to calibrate DFT-based structure prediction of the experimentally elusive **hs** states of **[FeL]$^{2+}$** and **[Fe(tren)py$_3$]$^{2+}$**. Based on an in-depth analysis of the calibration and prediction structure datasets, we suggest **hs**-state structures that show strong trigonal distortion in **[FeL]$^{2+}$** but are still in line with octahedral coordination in **[Fe(tren)py$_3$]$^{2+}$**. The respective zinc(II) complexes prove to be valid real-world structure models in both cases. Accordingly, the SCO reaction coordinates of both iron(II) complexes are concluded to be distinctly different, despite the largely conserved donor set and topology. Ligand-imposed trigonal torsion akin to the Bailar twist is evident in **[FeL]$^{2+}$**, but is absent in **[Fe(tren)py$_3$]$^{2+}$**. Divergence in the reaction coordinate is manifest in the SCO dynamics, as is consistently measured by laser flash photolysis and VT-NMR spectroscopy. The latter technique allows a direct phenomenological differentiation between "slowly" and "rapidly" exchanging SCO systems through qualitative inspection of NMR linewidths.

2. Results

2.1. Structural Characteristics of [FeL]$^{2+}$ and [ZnL]$^{2+}$

2.1.1. Complex Synthesis and Solid State Structures

Ligand **L** was prepared along a published route [25,30] by reaction of the thiophosphoryl hydrazide (S)P(N^{Me}NH$_2$)$_3$ with three equivalents pyridine-2-carbaldehyde in methanol. In situ complexation with the hexahydrates of iron(II) tetrafluoroborate and zinc(II) perchlorate affords deep red and colorless solutions, respectively, from which the products precipitate in good yields within hours. Elemental analysis indicates 1:1 metal ligand stoichiometry and the presence of ethanol as solvate. NMR spectra reveal (averaged) C_3 symmetry in both cases. A detailed discussion of the spectra is given below. Single crystals of **[FeL](BF$_4$)$_2$** and **[ZnL](ClO$_4$)$_2$** that were suitable for XRD structure elucidation were obtained from concentrated solutions in MeCN within few days via isothermal diffusion of diethyl ether. Both compounds crystallized as MeCN solvates. Crystallographic details are summarized in Table 1, pertinent structural features are given in Table 2.

The iron(II) complex crystallizes in the orthorhombic space-group type $P2_12_12_1$ with 1.5 MeCN molecules per complex. The asymmetric unit contains two complex units of complementary helicity. While the overall packing is unexceptional, we note π-stacking between pyridine moieties of two adjacent complex units and a dispersive interaction between the capping sulfur atom and a methyl group. The zinc(II) complex also crystallizes as MeCN solvate in the monoclinic space-group type $P2_1/c$. The solid-state structure lacks intermolecular interactions between complex cations. The cation structures are found to be distinctly dependent on the nature of the central ion (Figure 1; structure details in Table 2). The iron(II) complex reveals fairly regular N$_6$ coordination with little variation in the Fe–N bond lengths and only minor *cis*-angle distortion. The iron ion is well centered in the N$_6$ coordination sphere; the displacement δ is small. Its negative value signalizes displacement towards the "P(S)-clamped" side. An average Fe–N bond length of 1.952(15) Å indicates **ls** configuration of the d^6 ion, which is in agreement with ^{1}H-NMR resonances in the range of 9.0 ppm > δ > 2 ppm, typical of diamagnetic compounds. Projection of the coordination sphere along the (pseudo) C_3 axis reveals significant distortion from a regular octahedron (right in Figure 1). The trigonal twist angle θ was introduced by Hendrickson et al. in order to quantify such Bailar-type [28,36] distortions of L$_6$ coordination spheres. The trigonal twist angle θ amounts to 60° for a regular octahedron and gives 0° for a trigonal prism. With a value of θ = 43.4(8)°, the coordination pattern of **[FeL]$^{2+}$** is well within the range observed for **ls**-iron(II) complexes of N$_6$ ligands of the extended tripod type and closely mimics structure analogues with pyridine derivatives [26,51]. As the experimental data are closely matched by a DFT-derived vacuum structure of the isolated complex with respect to bond lengths and angles (see Table 2), only minor matrix effects may be expected. This conclusion is corroborated by crystallographic

work-in-progress, which indicates conserved complex metrics of **[FeL]²⁺** and **[ZnL]²⁺**, even when the counter ion is varied. It is emphasized, however, that matrix effects through counter ion variation or solvates commonly and strongly affect the phenomenology of SCO. Tris(2-picolylamine)iron(II) dichloride, for instance, may be **ls**, **hs** or undergo SCO, depending on the nature of co-crystallized alcohol in an unpredictable manner [52]. Accordingly, the trigonal twist angle θ of the **hs**-complex **[FeL']²⁺** was recently shown to be significantly biased by matrix effects, firstly causing some deviation of the DFT-derived and experimental values and, secondly, enhancing the susceptibility towards the counter-ion [27].
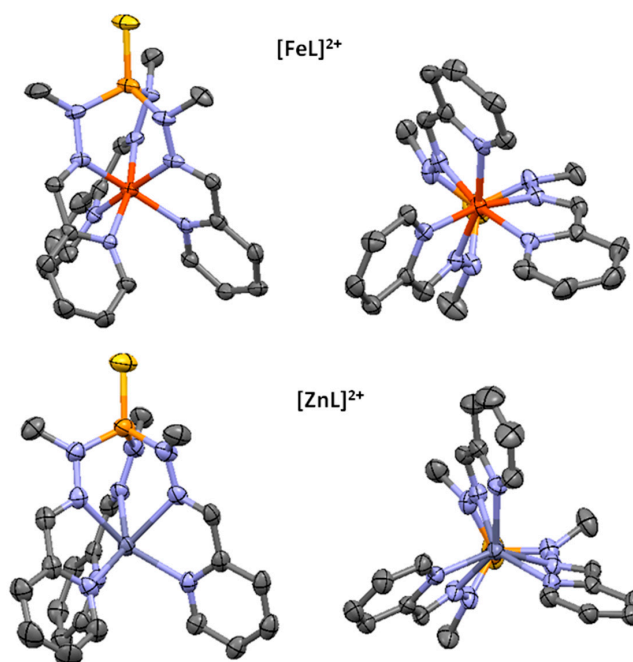
Figure 1. (**left**) Side views and (**right**) projections along M–P–S of molecular structures of (**top**) **[FeL]**(BF₄)₂ and (**bottom**) **[ZnL]**(ClO₄)₂. Ellipsoids of 50% probability; only the dicationic complexes are shown; counterions, solvent molecules, and hydrogen atoms have been omitted for clarity. Dark grey: carbon, blue: nitrogen, yellow: sulfur, light orange: phosphorous, dark orange: iron, light grey: zinc atoms.

Table 1. Crystallographic data.

Compound	[FeL](BF₄)₂·1.5 CH₃CN	[ZnL](ClO₄)₂·1.5 CH₃CN
Sum formula	$C_{24}H_{28.5}B_2F_8FeN_{10.5}PS$	$C_{24}H_{28.5}Cl_2N_{10.5}O_8PSZn$
M (g·mol⁻¹)	756.57	791.37
Shape and color	black plate	colorless column
Size (mm³)	0.41 × 0.31 × 0.16	0.44 × 0.25 × 0.21
crystal system	orthorhombic	monoclinic
space group	$P2_12_12_1$	$P2_1/c$
a (pm)	1134.21(5)	909.34(12)
b (pm)	1532.91(7)	3165.3(3)
c (pm)	3673.55(18)	1628.1(2)
α (°)	90	90
β (°)	90	136.39(3)
γ (°)	90	90

Table 1. *Cont.*

Compound	[FeL](BF$_4$)$_2$·1.5 CH$_3$CN	[ZnL](ClO$_4$)$_2$·1.5 CH$_3$CN
V (10^6 pm^3)	6387.0(5)	3232.2(19)
μ (mm^{-1})	0.671	1.104
$\rho_{calcd.}$ (g·cm^{-3})	1.574	1.626
Z	8	4
T (K)	150(1)	150(1)
2 θ_{max} (°)	52.00	52.00
reflns. Measured	27,331	24,831
reflns. Unique	12,295	6322
parameters/restraints	932/253	475/114
R_1 ($I \geq 2\sigma(I)$)	0.0578	0.0699
R_1 (all data)	0.0810	0.0820
wR_2 ($I \geq 2\sigma(I)$)	0.1078	0.1606
wR_2 (all data)	0.1180	0.1680
u, v	0.0427, 1.3949	0.0472, 12.7098
S	1.018	1.109
Flack parameter x	0.012 (12)	n/a
ρ_{max}/ρ_{min} ($e \times 10^{-6}$ pm^{-3})	0.50/−0. 53	0.99/−0.90
CCDC number	1564278	1564279

$w = [\sigma^2(F_o^2) + (uP)^2 + vP]^{-1}$ with $P = [\max(F_o^2, 0) + 2F_c^2]/3$.

Table 2. Pertinent geometric parameters ((average) bond lengths in Å; angles in °; standard deviations in parentheses) of the complexes **[FeL]$^{2+}$** and **[ZnL]$^{2+}$** from XRD analysis and DFT calculations (italicized). [a]

	[FeL](BF$_4$)$_2$	*ls*-[FeL]$^{2+}$	[ZnL](ClO$_4$)$_2$	[ZnL]$^{2+}$
distances (Å)				
d$_{Fe-N(ald)}$	1.924(7)	*1.930(1)*	2.244(16)	*2.254(2)*
d$_{Fe-N(py)}$	1.979(10)	*1.974(1)*	2.133(11)	*2.134(2)*
d$_{Fe-N}$	1.952(15)	*1.952(11)*	2.19(2)	*2.19(3)*
bite	2.520(6)	*2.535(2)*	2.657(4)	*2.677(1)*
Fe–P	3.123(3)	*3.162*	3.482(5)	*3.509*
h [b]	2.225	*2.216*	2.587	*2.586*
δ [c]	−0.017	*−0.014*	+0.425	*+0.389*
angles (°)				
cis N$_{ald}$–Fe–N$_{ald}$	90.4(9)	*90.6(1)*	79.8(6)	*81.2(2)*
cis N$_{py}$–Fe–N$_{py}$	91.1(14)	*91.2(1)*	97(3)	*95.9(1)*
bite angle	80.4(2)	*81.0(1)*	74.7(4)	*75.1(3)*
trans N$_{py}$–Fe–N$_{ald}$	166.2(12)	*167.7(1)*	145(2)	*148.1(2)*
distortion				
$\sum_{cis}$/° [d]	76.2	*57.9*	163.3	*164.4*
θ° [e]	43.4(8)	*45.0(1)*	19(2)	*22.3(1)*
S (O_h) [f]	1.464	*1.168*	8.613	*7.147*
S (TP) [f]	9.306	*10.007*	2.135	*2.700*

[a] Optimisation with BP86-D/TZVPP; [b] distance between the triangular faces of N$_{(ald)3}$ and N$_{(py)3}$; [c] metal displacement from the coordination center; [d] summed deviation from 90° of 12 N–Fe–N *cis* angles; [e] trigonal distortion ([22]); [f] continuous shape measures $S(O_h)$ and $S(TP)$ with reference to the centered octahedron and the centered trigonal prism, respectively ([40,42]).

Moderate trigonal distortion is a common structural feature when trigonally directing ligands are used [37]. This also becomes evident from an analysis in terms of the holistic continuous shape measures $S(O_h)$ and S(TP). These measures, as introduced by Avnir and Alvarez et al. [40,42], approach zero when the experimental structure is in good agreement with a reference polyhedron (in our case, O_h and TP denote the centered regular octahedron and the centered regular trigonal prism,

respectively). Clearly, **[FeL]$^{2+}$** with $S(O_\text{h})$ = 1.464 is well described by an octahedron with only moderate trigonal distortion.

Distortion from O_h of the coordination sphere of **[ZnL]$^{2+}$** is significantly stronger. Averaged trigonal twist angles amount to only 19(2)°, so that the coordination is rather describable as a moderately distorted trigonal prism. This conclusion is corroborated by the small value of the trigonal shape measure S(TP) = 2.135. In part, global distortion may be tracked to quite severe cis-angle distortion; in particular $\sum_\text{cis}$ of the zinc(II) congener strongly exceeds distortion in the iron(II) complex. Concomitant with cis-angle distortion, severe bending from 180° of the nominal trans-angles (N_py–Fe–N_ald) is observed, accompanied by significant variation of the Zn–N bond-lengths. As this variation is donor-type specific (d(Zn–N_ald) > d(Zn–N_py)), the result is an expulsion of the zinc ion to the "loose" end of the coordination sphere. The displacement from the center δ is large and it is positive. In this context, it is thus important to note that the displacement pattern observed for complexes of **L** (d(**[FeL]$^{2+}$** < 0; d(**[ZnL]$^{2+}$** > 0) is the opposite of that reported for complexes of **(tren)py$_3$** [53]. As noticed earlier [27], both ligands are members of distinctly different classes, owing to their different cap topologies. In particular, nominally hexadentate (heptadentate, if the apical nitrogen atom is considered) **(tren)py$_3$** rather consists of three largely independent diimine arms, giving 3 × 2 coordination [54].

hs-iron(II) [27] and zinc(II) complexes [31] with structure motifs akin to **[ZnL]$^{2+}$** have been previously received with ligands of the extended tripod type. The quite general surrogate function of zinc(II) for **hs**-iron(II) is clearly a result of the coinciding ionic radii of Zn^{2+} and **hs**-Fe^{2+}. In consequence, the structure of the elusive **hs**-state of **[FeL]$^{2+}$** must be expected to be strongly distorted towards a trigonal prism as well. This conclusion is fully corroborated by an XRD-calibrated DFT study (see below).

2.1.2. Complex Structures in Solution via ^{1}H-NMR Spectroscopy

The solid state structures of **[FeL]**(BF$_4$)$_2$ and **[ZnL]**(ClO$_4$)$_2$ revealed coordination units with approximate C_3 symmetry along the M–P–S vector. The occurrence of only a single set of resonances in the ^{1}H-NMR spectra indicates conserved symmetry in MeCN solution. While sharp resonances with resolved spin–spin coupling are recorded in the case of the zinc(II) complex, rather broad lines prevail at room temperature for most proton sites of the iron(II) complex (for proton assignment, see Scheme 1). Here spin–spin coupling is mostly blurred through severe line broadening, but becomes resolved upon decreasing the temperature. Low-temperature spectra recorded close to the freezing point of the solvent allowed unambiguous assignment. 2D-COSY spectra recorded in [D$_3$]MeCN at room temperature are shown in Figure 2 (region of resonances of aromatic protons, H$^{1-4}$ and H^5). Besides the aforementioned differences in line width, the quite different spectral widths and the diverging peak positions deserve attention.

The resonances of the zinc(II) complex assemble in a very dense pattern, covering a chemical shift range Δδ of only 0.54 ppm. The spectral width is significantly smaller than the widths reported by Breher et al. [29] for both the free ligand (Δδ = 1.30 ppm) and the respective copper(I) complex (Δδ = 1.15 ppm). By contrast, the resonances of the aromatic protons (and H^5) of the iron(II) complex are spread out over a 2.11 ppm range. The increase in spectral width is mainly associated with the peak position of the ortho-proton resonance (H^1), which is located at 8.12 ppm and 6.52 ppm for the zinc and the iron complex, respectively. The substantial upfield shift, also with respect to the free ligand, points to a structure imposed origin. Actually, the crystal structure of **[FeL]**(BF$_4$)$_2$ reveals close contacts of H^1 and nitrogen atoms of a neighboring pyridine (d(H^1···N) ≈ 2.5 Å) allowing efficient spatial overlap with its π-system. In turn, the lowfield positioned resonance of H^1 in the zinc complex indicates the lack of anisotropy effects and, therefore, the lack of close contacts of H^1 and other pyridine units. This is in agreement with the crystal structure of **[ZnL]**(ClO$_4$)$_2$, where d(H^1···N) ≈ 2.9 Å and H^1 is fully displaced from the aromatic ring plane of neighboring pyridine. We conclude that the structures of both complexes as found in the crystal are largely conserved upon dissolving the complex salts in

MeCN. We further conclude that the solution structures of the **ls**-iron(II) complex **[FeL]$^{2+}$** and of the **hs**-iron(II) surrogate **[ZnL]$^{2+}$** are distinctly different.
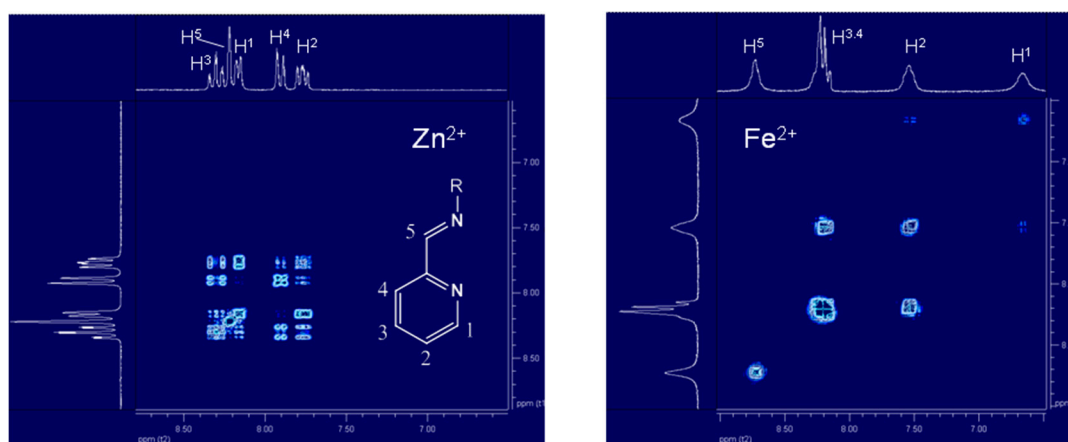
Figure 2. ^{1}H-NMR COSY spectra (200 MHz; D$_3$-MeCN) at ambient temperature; (**left**) **[ZnL]**(ClO$_4$)$_2$; (**right**) **[FeL]**(BF$_4$)$_2$; inset: assignment of proton sites.

### 2.1.3. DFT Structure Elucidation of Elusive **hs-[FeL]$^{2+}$**

While the ls-iron(II) complex of **L** could be structurally characterized by XRD crystallography, only indirect structure information of the elusive **hs**-state is available. In particular, the trigonally distorted structure of the respective zinc(II) complex suggests similar metrics of **hs-[FeL]$^{2+}$**. In order to validate this hypothesis, the structure variability of the iron(II) and zinc(II) complexes of **L** was investigated with DFT methods and calibrated by XRD data as far as possible. A comparison of XRD-derived data and complex metrics from DFT data (BP86-D/TZVPP) is given in Table 2. Very good agreement among both datasets is obtained with respect to all pertinent bond lengths, non-bonding distances, bond angles and several measures of complex distortion (results of a functional scan for **ls-[FeL]$^{2+}$** are summarized in Table S1). The successful modeling of **ls-[FeL]$^{2+}$** and **[ZnL]^2** encouraged a DFT-based structure prediction of **hs-[FeL]$^{2+}$** that has been performed by use of a variety of functionals, in order to judge the reliability of the overall prediction and the robustness of the metrical parameters. Pertinent structural data of **hs-[FeL]$^{2+}$** are compiled in Table 3. Data for the reference systems **ls-[Fe(tren)py$_3$]$^{2+}$** and **hs-[Fe(tren)py$_3$]$^{2+}$** are given in Tables S2 and S3.

Table 3. Pertinent geometric parameters of DFT-optimized **hs-[FeL]$^{2+}$**.

	B3LYP a_0 [a] =						BP86	PBE	TPSS0	TPSSh
	0.00	0.05	0.10	0.15	0.20	0.25				
Bond lengths [Å]										
$d_{Fe-N(ald)}$	2.197	2.211	2.226	2.230	2.238	2.253	2.199	2.200	2.205	2.198
$d_{Fe-N(py)}$	2.132	2.150	2.169	2.175	2.186	2.198	2.134	2.138	2.161	2.152
d_{Fe-N}	2.164	2.181	2.198	2.203	2.212	2.225	2.167	2.169	2.183	2.175
distortion										
$\sum_{cis}$/° [b]	150.1	154.7	160.2	161.2	163.9	171.2	150.5	151.2	159.8	155.6
θ/° [c]	24.0	22.2	20.5	20.3	20.2	17.8	24.3	24.3	20.4	21.5
$S(O_h)$ [d]	6.54	7.13	7.78	7.86	7.91	8.92	6.51	6.45	7.82	7.39
$S(TP)$ [d]	3.09	2.66	2.27	2.24	2.24	1.79	3.12	3.19	2.24	2.48

[a] amount of exact exchange; [b] summed deviation from 90° of 12 N–Fe–N *cis* angles; [c] trigonal distortion ([22]); [d] continuous shape measures $S(O_h)$ and $S(TP)$ with reference to the octahedron and the trigonal prism, respectively ([40,42]).

While a certain functional-imposed bias on the bond lengths and the distortion measures of **hs-[FeL]$^{2+}$** cannot be denied (similar conclusions hold for the other iron(II) complexes under study), the overall appearance of the coordination sphere is independent of the functional. All optimizations of **hs-[FeL]$^{2+}$** consistently reveal substantial trigonal tortion towards prismatic coordination (averaged across all functionals, θ amounts to 21.6(7)°). Notably, the range of the trigonal twist angles matches the respective value of the zinc(II) congener. Furthermore the averaged Fe–N bond lengths of the **hs**-iron(II) complex (d(Fe–N) = 2.188(7) Å) very well match the bond lengths of the zinc(II) complex (d(Zn–N) = 2.194 Å). Finally, the small values of the trigonal shape measures (S(TP) = 2.53(20)), again akin to **[ZnL]$^{2+}$** with S(TP) = 2.70, clearly prove **[ZnL]$^{2+}$** to be a convincing structure model of the **hs**-iron(II) complex and assign **hs-[FeL]$^{2+}$** as a trigonal prismatic complex (Figure 3a).
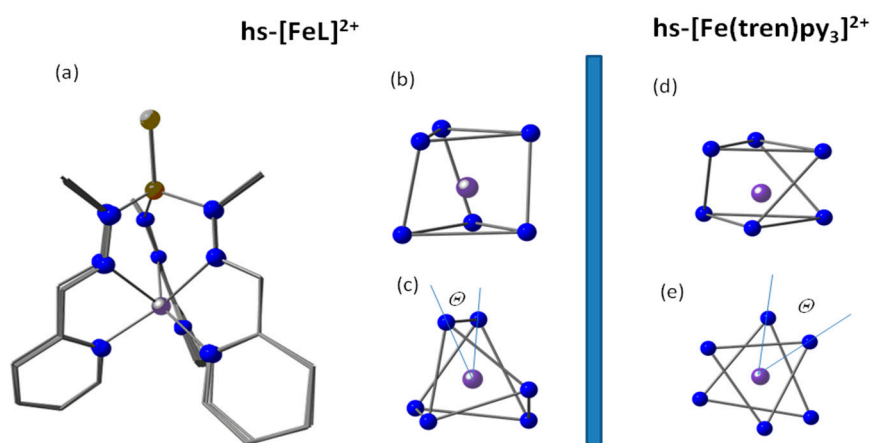
Figure 3. (**a**) Side view of the merged DFT-derived structures of **hs-[FeL]$^{2+}$**; (**b**) side view and (**c**) top view along S–P–Fe of the [FeN$_6$] coordination sphere (BP86-D/TZVPP); (**d**,**e**) show side and top view along of the [FeN$_6$] coordination sphere of **hs-[Fe(tren)py$_3$]$^{2+}$** (BP86-D/TZVPP).

Comparison with the optimized **hs**-structures of the well-established reference compound **[Fe(tren)py$_3$]$^{2+}$** reveals a much weaker tendency towards the trigonal prism (Figure 3b; Tables S2 and S3). Averaged over all optimized structures, θ amounts to 47.1(4)°. Again there is very close agreement among the metrics of the optimized iron(II) complex and the data of the respective zinc(II) complex, both from DFT (θ = 46.3°) and XRD (θ = 45.9°; from [53]), further supporting the structure proposal for elusive **hs-[Fe(tren)py$_3$]$^{2+}$**. The conclusion of a structure conserving SCO is obvious for **[Fe(tren)py$_3$]$^{2+}$**: Shuttling between the **ls** and the **hs** states of this complex induces the typical expansion/contraction of the coordination sphere by ≈0.2 Å for each Fe–N bond, but leaves the overall shape and appearance of the coordination unit greatly unaffected (apart of the spin-state dependence of the apical Fe–N$_7$ distance). Accordingly, **[Fe(tren)py$_3$]$^{2+}$** is well modeled by an ideal octahedron in both spin states, as can be read from the small values of the octahedral shape measures (**ls**: S(O_h) = 0.65(5); **hs**: S(O_h) = 2.12(4)).

2.2. DFT-Derived SCO Energies of [FeL]$^{2+}$ and [Fe(tren)py$_3$]$^{2+}$

Previous DFT work on the SCO energies of iron(II) complexes of some extended-tripod ligands has revealed matching **ls-hs** energy spacing within the couple **[FeL′]$^{2+}$** and **[Fe(tren)imid$_3$]$^{2+}$** [27]. On the B3LYP*-D/TZVP level of theory (amount of exact exchange a_0 = 0.15), the apparent SCO energies of these complexes were identical within DFT accuracy ($\Delta_{SCO}E = E$(**hs**) − E(**ls**); positive values of $\Delta_{SCO}E$ indicate a **ls** ground state). Experimental results from VT-UV-Vis spectroscopy corroborated the proximity of the SCO energies. As a matter of fact, the apparent SCO energies of **[FeL]$^{2+}$** and **[Fe(tren)py$_3$]$^{2+}$** obtained in this work likewise match, when computed on the B3LYP*-D/TZVPP level of theory (Table 4). Comparison with the reference systems indicates significantly higher SCO energies, pointing to greatly favored **ls**-states and higher SCO transition temperatures, $T_{1/2}$. This qualitative

conclusion is fully supported by the experimental properties of both compounds. XRD data are in line with **ls**-complexes in the crystal at 150 K, whereas NMR and UV-Vis spectroscopy consistently rule out more than very minor **hs**-contributions in solution around room temperature.

In order to avoid overemphasizing of the B3LYP*-derived data, we have undertaken more extensive evaluations of the SCO energies via variation of the amount of exact exchange of the parent B3LYP functional within $0.00 < a_0 < 0.20$, both for the calibration couple **[FeL']$^{2+}$**/**[Fe(tren)imid$_3$]$^{2+}$** and for the prediction couple **[FeL]$^{2+}$**/**[Fe(tren)py$_3$]$^{2+}$** (Table 4). Electronic energies *E* are reported throughout. Although harmonic frequencies have been computed for all complexes, we refrain from using DFT-derived entropies $\Delta_{SCO}S$ to adjust the scale to free energies, $\Delta_{SCO}G$. Plots of the derived apparent SCO energies of the four complexes against a_0 are convincingly linear as is generally observed [55–58], showing structure-independent slopes but structure-dependent offsets (Figure S1, in Supplementary Materials). Across the a_0 scan, we consistently find the **ls** forms of **[FeL]$^{2+}$** and **[Fe(tren)py$_3$]$^{2+}$** favored versus their reference compounds by 24(1) kJ·mol^{-1} and 27(1) kJ·mol^{-1}, respectively. Reasonably assuming similar SCO entropies of $\Delta_{SCO}S \approx 80$ J·(K·mol)$^{-1}$, among this set of structurally related complexes, transition temperatures $T_{1/2} > 450$ K are expected for **[FeL]$^{2+}$** and **[Fe(tren)py$_3$]$^{2+}$**. These assumptions are corroborated by VT-UV-Vis and VT-NMR spectroscopy.

Table 4. Functional scan of apparent SCO energies of iron(II) complexes from Scheme 1. [a]

	$\Delta_{SCO}E$ (kJ·mol^{-1})				
	a_0 [b] = 0.00	0.05	0.10	0.15	0.20
[FeL]$^{2+}$	153.4	116.7	79.4	46.6	10.3
[Fe(tren)py$_3$]$^{2+}$	154.2	116.3	80.0	46.2	14.8
[FeL']$^{2+}$	127.7	89.7	54.1	21.2	−9.0
[Fe(tren)imid$_3$]$^{2+}$	123.3	87.3	52.8	20.5	−9.0

[a] Structures fully optimized with B3LYP-D/TZVPP; $0.00 < a_0 < 0.20$; [b] amount of exact exchange.

2.3. Dynamics of SCO in *[FeL]$^{2+}$* and *[Fe(tren)py$_3$]$^{2+}$*

2.3.1. Optical Spectroscopy

[FeL](BF$_4$)$_2$ and **[Fe(tren)py$_3$]**(ClO$_4$)$_2$ give deeply red and purple solutions. The colors correspond to intense absorption bands ($\varepsilon_{max} > 8000$ cm^{-1}·M^{-1}) at $\lambda = 500$ nm and $\lambda = 560$ nm, respectively. As is typical for combinations of iron(II) with π-accepting ligands, the Vis transitions can be associated with charge transfer from the iron(II) center to the ligand (MLCT). As is shown via VT-UV-Vis spectroscopy of solutions of **[FeL]**(BF$_4$)$_2$ in MeCN ($T_{max} = 345$ K), the MLCT transition is only marginally affected at elevated temperature (Figure S2). That is, peak position and intensity are conserved, with a very slight intensity loss of <5% at the highest available temperature. This observation points to high-lying SCO transition temperatures, in agreement with the predictions from DFT.

Previous work has shown that MLCT excitation of **ls**-iron(II) gives the meta-stable **hs**-state in a selective way. Ultra-fast depopulation of the MLCT-like Franck-Condon state concomitant with quintet-state population generally occurs on the sub-ps timescale, greatly independent of ligand nature. Accordingly, the MLCT-state in a structure analogue of **[FeL]$^{2+}$** is depopulated within few hundreds of femtoseconds [26]. We note in passing that there is much current interest in "taming" of MLCT states, aiming at longer MLCT-state lifetimes [24,59,60]. Laser-flash photolysis is therefore used to drive the SCO equilibrium (Equation (1)) towards the **hs**-state by means of a short-lived photochemical stimulus. Recovery of the equilibrium is recorded via transient absorption spectroscopy [13–24]. This acquisition scheme has been shown previously to be applicable for a number of iron(II) complexes [25–27]. Transient-absorption spectra recorded directly after ns-laser excitation of solutions of **[FeL]**(BF$_4$)$_2$ and **[Fe(tren)py$_3$]**(ClO$_4$)$_2$ in MeCN and MeOH are shown in Figure 4a. Owing to the spectral transparency of the **hs**-state in the Vis regime, the transient spectra are dominated by diagnostic bleach signals ($\Delta A < 0$), which reflect the positions and relative intensities of the peaks in the ground

state absorption spectra. Additional transient absorbance ($\Delta A > 0$) appears in the spectra of **[FeL]**(BF$_4$)$_2$ in the near-UV region. This feature may be associated with the MLCT transition of the meta-stable **hs**-state. In the spectra of **[Fe(tren)py$_3$]**(ClO$_4$)$_2$ such transient absorption below 400 nm is absent; bleaching extends all over the spectrum. Different from **[FeL]**(BF$_4$)$_2$ the tren-derivative exhibits an additional intense MLCT-like transition in this spectral region. Bleaching of this intense transition through **ls** depopulation obviously outweighs the MLCT contribution of the meta-stable **hs**-state. Both the transient spectra and decay kinetics are only marginally affected by the solvent. I.e., the spectra recorded in MeOH and MeCN match almost ideally (squares and circles in Figure 4a). There is no spectral evolution during the course of transient decay. Decay profiles can be convincingly fitted to single-exponential decay functions, with time constants that are independent of the wavelength across the complete spectrum. The return to baseline absorption points to highly reversible photophysics and is in line with the implications of photo-induced SCO.
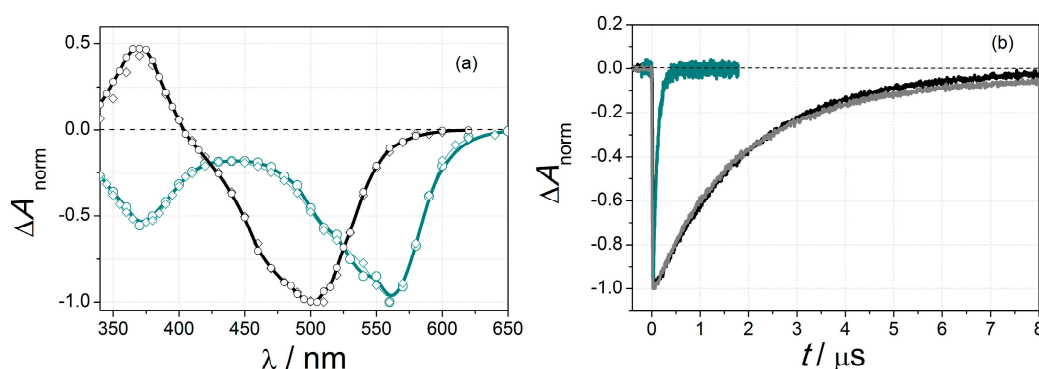
Figure 4. (**a**) Normalized transient absorption spectra recorded directly after laser excitation at 532 nm (MeOH; T = 298 K; $I_{exc} \approx 3$ mJ; fwhm ≈ 9 ns): **[FeL]$^{2+}$** (OD$_{532}$ = 0.36; black) and **[Fe(tren)py$_3$]$^{2+}$** (OD$_{532}$ = 0.15; green); additional data recorded in MeCN are given as square symbols; (**b**) transient decay profiles recorded at 500 nm for **[FeL]$^{2+}$** (black: MeOH; grey: MeCN) and at 560 nm for **[Fe(tren)py$_3$]$^{2+}$** (green).

The lifetimes of transient decay, τ_{obs} ($\tau_{obs}^{-1} = k_{obs} = k_{H \to L} + k_{L \to H}$; $k_{H \to L}$ and $k_{L \to H}$ denote the rate constants of the **hs**→**ls** and the **ls**→**hs** transitions, respectively) are obtained from mono-exponential fits of the experimental data at variable temperature. As both compounds under study are **ls**-compounds with very small contributions of the **hs**-state at experimentally available temperatures, it becomes $k_{L \to H} << k_{H \to L}$, so that $k_{obs} \approx k_{H \to L}$. That is, the decay profiles in the transient absorption spectra are fully dominated by the relaxation of the *minority* component. It is noted at this point that intrinsically slower techniques may allow an ad-mixing of the decay of the majority component (see the NMR discussion below).

Table 5. Pertinent results from LFP of the iron(II) complexes in MeCN.

	[FeL]$^{2+}$	**[Fe(tren)py$_3$]$^{2+}$**
E_a [kJ·mol^{-1}]	22(1) [a]	7.8(3) [b]
$k_{H \to L}$ [10^6 s^{-1}] [b]	0.46	15.9
$k_{L \to H}$ [10^6 s^{-1}] [c]	<0.005	<0.2

[a] thermal barriers of 21.9 ± 0.3, 21.6 ± 0.3 and 20.9 ± 0.6 kJ·mol^{-1} have been recorded in MeOH, dichloromethane and water, respectively [25]; [b] measured in acetone, taken from [43]; decay rate constant at room temperature; [c] estimated with $K_{SCO} = \gamma_{hs}/\gamma_{ls} < 0.01$ at room temperature.

Notably the decay dynamics differ considerably among both compounds (Figure 4b). The decay rate constant $k_{obs} = 1.6 \times 10^7$ s^{-1} of **[Fe(tren)py$_3$]**(ClO$_4$)$_2$ is in qualitative agreement with previous measurements in acetone [43]. Decay of **[FeL]**(BF$_4$)$_2$ is substantially slower, yielding a decay rate

constant of $k_{obs} = 4.6 \times 10^5$ s^{-1}. The sharp difference in the decay dynamics of both compounds is attributed to distinctly different activation barriers. Arrhenius treatment of the rate constants of **[FeL]$^{2+}$** measured within a temperature range 250 K $< T <$ 320 K gives a linear plot, ln(k_{obs}) vs. $1/T$ (Figure S3). A thermal barrier of $E_a = 22.2$ kJ·mol^{-1} is extracted in MeCN solution (Table 5), which well compares with previous experiments in other solvents, but deviates strongly from the reported value of $E_a = 7.8$ kJ·mol^{-1} of **[Fe(tren)py$_3$]$^{2+}$**. It is noted that our data on **[Fe(tren)py$_3$]$^{2+}$**, admittedly preliminary, indicate a somewhat stronger temperature dependence of its spin-state relaxation: While we obtain perfect agreement with the reported rate constants at $T = 260$ K, we record a lifetime of 65 ns at 293 K, which is significantly shorter than Hendrickson's 95 ns. With our preliminary data, we estimate $E_a \approx 12$ kJ·mol^{-1}, which appears to be in closer agreement with NMR-derived dynamics (see below). A more extended LFP study will of course be required to validate our result. Suffice to state here that the thermal barrier in **[Fe(tren)py$_3$]$^{2+}$** will be around 10 kJ·mol^{-1}.

Although the solvent properties in the series MeCN, MeOH, water, dichloromethane vary widely (polarity, hydrogen bonding, internal pressure), the thermal SCO barriers of **[FeL]$^{2+}$** are identical within experimental error. The indifference of the SCO kinetics to solvent properties is in line with an inherently small solvent dependence of the SCO phenomenon deduced by Navon, Bixon and Jortner from statistical arguments already in 1980 [61]. A major steering effect of the solvent on the SCO thermodynamics has been recently reported by Halcrow et al. and Petzold et al., though [62,63]. In both cases, strong effects of solvent-complex hydrogen bonding were invoked to rationalize the results. Respective effects on the SCO kinetics of these systems have not been reported yet. In this context, it is interesting to note that the SCO kinetics of a hydroxyl-substituted congener of **[FeL]$^{2+}$** have been previously found to vary significantly with solvent [26].

2.3.2. VT-NMR Spectroscopy

The above results of optical spectroscopy in concert with the large preference for the **ls**-state in DFT are manifest also in the room temperature ^{1}H-NMR spectra in [D$_3$]MeCN of **[FeL]$^{2+}$** and **[Fe(tren)py$_3$]$^{2+}$**. The resonances cover the range typical of diamagnetic compounds (9 ppm $> \delta >$ 1 ppm) and they largely stay in this region irrespective of temperature. Figure 5a highlights the temperature dependence of the "aromatic proton" region of **[FeL]$^{2+}$** in [D$_3$]MeCN between 245 K $<$ T $<$ 340 K, measured at a frequency of 400 MHz. Evidently temperature has little effect on the peak positions, shifting the resonances by, at most, 0.6 ppm across the temperature range (Figure 5b). The sign and the relative size of the temperature induced shifts correlate with the residual spin density on the respective proton sites (from DFT studies). This points to a slight growing-in of **hs**-species at elevated temperatures. Measurements at even higher temperatures in [D$_5$]nitrobenzene at 500 MHz corroborate the picture of a beginning SCO with still minor contributions of the **hs**-species (Figure S4); by contrast, in pure **hs** complexes of polypyridine ligands, ortho-proton resonances are typically low-field shifted beyond $\delta >$ 50 ppm. For instance, the ortho-proton resonance of **[FeL']$^{2+}$**, which is **hs** in [D$_3$]MeCN at all accessible temperatures, was recorded at $\delta=$ 82 ppm at T = 295 K [27]. A maximum shift of the H^1 resonance in **[FeL]$^{2+}$** by $\Delta\delta = 6$ ppm at close to 400 K therefore refutes contributions of the **hs**-state exceeding $\gamma_{hs} > 0.10$. Largely the same observations are made for solutions of **[Fe(tren)py$_3$]$^{2+}$** in [D$_5$]nitrobenzene (500 MHz), although the thermal shift of some protons is somewhat larger (H^5; $\Delta\delta = 9$ ppm; Figure S5). Taken together, the observations fully support the prediction of high-lying SCO transition points at T$_{1/2}$ > 450 K in both compounds. We note further that the datasets of **[FeL]$^{2+}$** in [D$_3$]MeCN and [D$_5$]nitrobenzene nicely overlap (H^1; filled and open symbols in Figure 5b; a Curie plot of the chemical shifts is given in Figure S6), ruling out significant ligand-structure effects of the SCO thermodynamics.
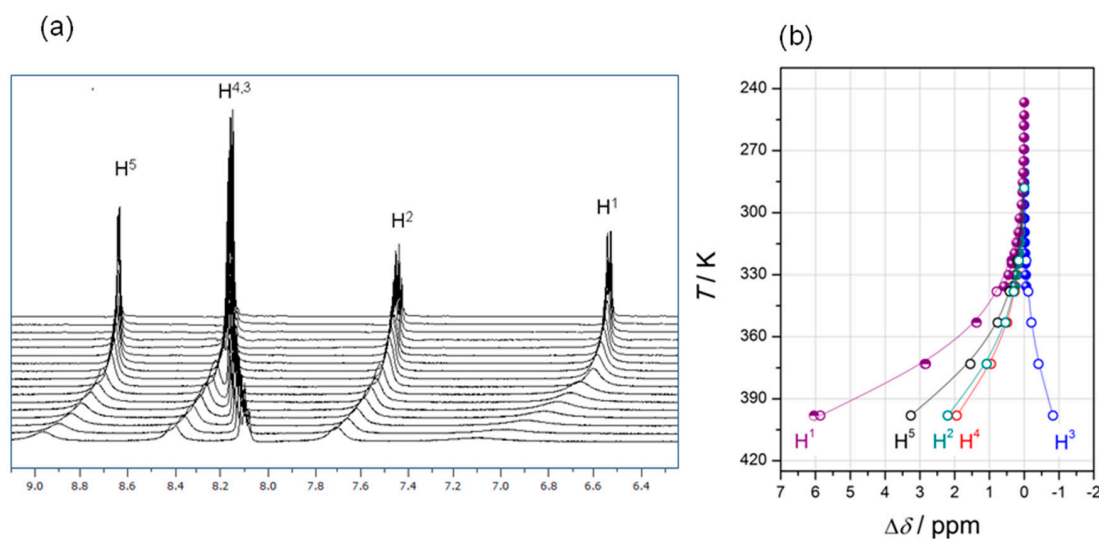
Figure 5. (**a**) VT-^{1}H-NMR spectra of **[FeL]**(BF$_4$)$_2$ (400 MHz; [D$_3$]MeCN; zoom on "aromatic protons"; intensities are not to scale; (**b**) temperature-dependent drift of resonances due to H$^{1-5}$ in **[FeL]**(BF$_4$)$_2$ (for proton assignment, see Scheme 1); open symbols: **[FeL]**(BF$_4$)$_2$ (500 MHz; [D$_5$]nitrobenzene); half-filled symbols: **[Fe(tren)py$_3$]**(ClO$_4$)$_2$ (H^1; 500 MHz; in [D$_5$]nitrobenzene).

Only at temperatures close to the freezing point of MeCN the spin–spin coupling in **[FeL]$^{2+}$** is resolved. By contrast, the resonance of H^1 in **[Fe(tren)py$_3$]$^{2+}$** is already well resolved at 288 K (500 MHz). The spectral information is in both cases progressively lost upon increasing the temperature: The moderate temperature-induced drift of the resonances is accompanied by substantial broadening of the resonances in both complexes, however, with significantly sharper lines in **[Fe(tren)py$_3$]$^{2+}$** at all temperatures. Notably, the extent of line broadening of **[FeL]$^{2+}$** at a given temperature increases with the Larmor frequency. At $T = 298$ K, the linewidth of the H^1 resonance in **[FeL]$^{2+}$** (*LW*, full-width at half maximum) amounts to 19 Hz, 34 Hz and 42 Hz (the latter value at $T = 288$ K), when measured at 200 MHz, 400 MHz and 500 MHz, respectively. The field dependence points to a dynamic origin of the line broadening. In previous work on bis-meridional coordinated iron(II) complexes [63–65], we have recorded field-dependent NMR line broadening, which could be quantitatively analyzed in terms of a two-sites chemical exchange model. In particular, the linewidths could be correlated with the kinetics of SCO ($k_{obs} = k_{L \to H} + k_{H \to L}$). In the fast-exchange limit of a two-sites model, chemical exchange distinctly contributes to the transverse relaxation time R_2 and, thus, to the linewidth *LW* ($R_2 = \pi \times LW$). The R_2 values can be approximated from Equation (2) with $\Delta\omega_H = (C^0/T + C^1) \times \omega$ ($\Delta\omega_H$ denotes the difference in proton Larmor frequency of **ls** and **hs** state; C^0 and C^1 denote the Curie constant and its first-order correction).

$$R_2 = \left\{ (1 - \gamma_{hs}) R_{2(ls)} + \gamma_{hs} \cdot R_{2(hs)} \right\} + \left\{ \gamma_{hs}(1 - \gamma_{hs}) \frac{\Delta\omega^2}{k_{obs}} \right\} \tag{2}$$

As such the NMR method requires knowledge of the chemical shifts of the (elusive) **ls** and **hs** state (C^0 and C^1) and the thermodynamic parameters of SCO ($\Delta_{SCO}S$ and $\Delta_{SCO}H$). In the current case of **[FeL]$^{2+}$** and **[Fe(tren)py$_3$]$^{2+}$**, however, some simplifying assumptions are possible. Both compounds are (close to) entirely **ls** at room temperature, so that the second term in Equation (2) can be approximately neglected, as long as the temperature remains well below $T_{1/2}$. In a second step, the first term is taken to be independent of temperature, so that all temperature dependence now resides in the third term of Equation (2). With these assumptions and simplifications, we derive Equation (3), which quantifies the change of R_2 relative to the pure **ls** state ($\Delta R_2 \approx R_2 - R_{2(ls)}$).

$$\Delta R_2 \approx \gamma_{hs}(1 - \gamma_{hs})\frac{\Delta\omega^2}{k_{obs}} \tag{3}$$

With this simplified equation in hands, two aspects deserve attention. Firstly, the temperature dependence of the transverse relaxation and therefore of *LW*, must be expected to have a bell-like shape (γ_{hs} (1 − γ_{hs}), maximum at $T = T_{1/2}$). As the factor ($\Delta\omega^2/k_{obs}$) decreases continuously with increasing temperature, the maximum linewidth LW_{max} is located at $T_{max} < T_{1/2}$. Such bell-shaped *LW* versus *T* plots in the NMR spectra of bis-meridional coordinated iron (II) complexes have been recently reported by us together with a detailed analysis in terms of admixed SCO dynamics [63,64]. While, in principle, each of the parameters γ_{hs}, $\Delta\omega$ and k_{obs} in Equations (2) and (3) must be considered structure-dependent, the coinciding SCO energies $\Delta_{SCO}E$ from DFT (Table 4) and the close similarity of the temperature drift in the NMR spectra of **[FeL]²⁺** and **[Fe(tren)py₃]²⁺** (Figure 5b), rule out significant ligand-structure imposed differences in γ_{hs} and $\Delta\omega$. That is, within this couple of complexes, effects of the SCO dynamics on the NMR linewidths are expected to be effectively isolated from other structural effects.
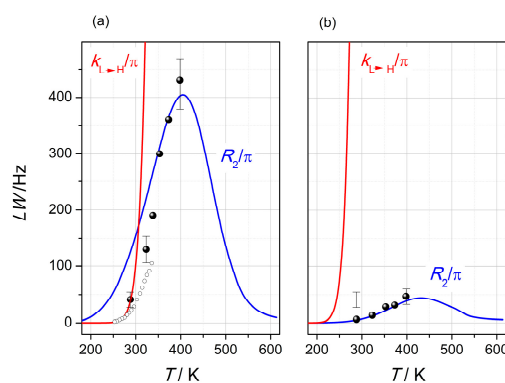
Figure 6. Temperature-dependent ¹H-NMR linewidths of proton H¹; filled symbols: 500 MHz; [D₅]nitrobenzene; open symbols: 400 MHz; [D₃]MeCN; blue lines: Model calculations of ¹H-NMR linewidths ($LW = R_2/\pi$) in terms of Equation (2) ($\Delta_{SCO}H = 40$ kJ·mol⁻¹; $\Delta_{SCO}S = 80$ J·(K·mol)⁻¹; C^0 = 40000 ppm·K; Arrhenius frequency factor: $A_{0(H\to L)} = 4 \times 10^9$ s⁻¹; 500 MHz); red line: temperature dependence of the **ls** relaxation rate constants $k_{L\to H}/\pi$ (Arrhenius frequency factor: $A_{0(L\to H)} = 6 \times 10^{13}$ s⁻¹); (**a**) **[FeL]**(BF₄)₂ with $E_a = 22$ kJ·mol⁻¹; (**b**) **[Fe(tren)py₃]**(ClO₄)₂: $E_a = 12$ kJ·mol⁻¹.

Model calculations of the linewidths of H¹ in **[FeL]²⁺** and **[Fe(tren)py₃]²⁺** in terms of Equation (2), with reasonable estimates of $\Delta\omega$ and k_{obs}, show that this is actually the case and corroborate the validity of the simplifications leading to Equation (3). Thereby $\Delta_{SCO}H$ was fixed at 40 kJ·mol⁻¹ (assuming $\Delta_{SCO}S = 80$ J·(K·mol)⁻¹, this corresponds to $T_{1/2} = 500$ K), while the Arrhenius barrier of the **hs** relaxation was allowed to vary between 22.0 kJ·mol⁻¹ (as measured for **[FeL]²⁺**) and 12.0 kJ·mol⁻¹ (as estimated for **[Fe(tren)py₃]²⁺**). A comparison of the measured linewidths and the modeling results in Figure 6 illustrates the impact of the SCO dynamics on the NMR linewidth. In particular, we find very close agreement between experiment and model for **[Fe(tren)py₃]²⁺** (Figure 6b). Fair qualitative agreement also prevails for **[FeL]²⁺** (Figure 6a) at higher temperatures. This overall agreement corroborates the underlying two-site model. Furthermore it gives indication of how strongly the differences in SCO dynamics can translate into NMR parameters. In turn, the SCO kinetics may be qualitatively estimated from NMR linewidths, provided that the inherent assumptions of Equation (2) are valid across the complete temperature range. In this respect we note an obviously sharper decrease of the linewidths in **[FeL]²⁺** below 340 K. I.e., at lower temperatures, the two-site model systematically overestimates the linewidths. Such deviations have been observed previously [64,65]. They have been attributed to the breakdown of the fast-exchange approximation inherent to the two-site model, rendering Equation (2) invalid at lower temperatures. In agreement with this notion, the experimental

linewidths (400 MHz; open symbols in Figure 6a) well match the relaxation kinetics of the **ls** state at $T < 300$ K (red curve in Figure 6a). Both the observation of large maximum linewidths and the deviation from the two-site model at low temperature are fully in line with inherently slow SCO dynamics in **[FeL]$^{2+}$**. In other words, the linewidths progressively reflect the dynamics of the majority spin state as soon as the SCO kinetics approaches the upper time limit of the NMR method; that is, time averaging among the spin states is lifted.

3. Discussion

Functional materials built from switchable molecular units are currently intensely sought after. Among the viable building blocks for such materials, SCO compounds based on iron(II) complexes hold high potential for the following reasons. Firstly, iron(II) complexes provide the largest magnetic change due to SCO; that is, $S_{hs} - S_{ls} = 2$. Secondly, in many cases the magnetic switching is accompanied by sharply varied optical response in the visible spectral regime, typically shuttling between deeply colored **ls** and faint or colorless **hs** states. Thus, thirdly, the systems are thermochromic and exhibit (after Vis excitation) negative photochromism; that is, iron(II) SCO complexes are photonically addressable. Finally, the wealth of experimentally accessible systems based on iron(II) provides a stable phenomenological background for structure prediction and search. One of the most significant drawbacks of iron(II)-based SCO compounds is their inherent kinetic lability towards thermal spin-state scrambling. In other words, an individual molecule in the **ls** state that can in principle be selectively addressed and driven to the **hs** state will lose its individuality spontaneously, and it will do so rapidly. In consequence, discrete spin states stable towards thermal randomization require either supramolecular concatenation via cooperative effects, cryogenic temperatures (LIESST effect) or sufficiently high thermal barriers.

While the first two alternatives have been studied with high intensity, the latter point attracted significantly less attention, although the concept of tuning of the SCO reaction coordinate points back to the late 1960s and has been recurrently discussed ever since [22]. The SCO reaction coordinate can be, in many cases, approximated as a (fully symmetric, isotropic) breathing of the coordination sphere (single-configurational coordinate model). This situation is represented by the parabolas given in black and red in Figure 7a. The **hs** parabola is shifted rightward with respect to the **ls** parabola along the reaction coordinate by a certain factor q, which mainly reflects the spin-state dependence of the metal-donor bond lengths. The horizontal shift of the parabolas establishes a thermal barrier E_a that has to be overcome during SCO. Notably for FeN$_6$ coordination compounds, if the isotropic model were strictly valid (which is not the case), both the shift factor q and the thermal barrier E_a become largely independent of ligand nature [11]. The only remaining option to tune and optimize the thermal barrier then is the variation of the driving force of SCO [61]. This option, favorably applied within complex families is represented by a green parabola in Figure 7a. Tuning of the reaction coordinate in this context therefore necessarily means to add an anisotropic component to the SCO induced molecular motion. Besides the coupled radial and angular motion in the hallmark system [Fe(tpy)$_2$]$^{2+}$ [11,66–69], which has profound consequences for the SCO dynamics, only very few other systems have been reported to couple the breathing motion to other vibration or torsion modes. Based on a XRD-calibrated DFT study of iron(II) complexes, we have recently suggested that the coordinate of SCO is heavily affected by the nature of the ligand. That is, ligands of the extended-tripod type may impose a structural bias that distorts the **hs**-coordination sphere towards the trigonal prism. As is shown in Figure 7a in terms of the emblematic picture of intersecting parabolas, such additional structural changes will directly affect the reaction coordinate and, in consequence, will massively affect the thermal barrier (blue in Figure 7a).

This conclusion is fully corroborated by the results of the present study, as outlined above. The iron(II) complex of ligand **L** is clearly defined as being **ls**, having only slightly distorted octahedral N$_6$ environment. DFT optimization gives consistent results. The very same holds for the well-established **ls**-complex **[Fe(tren)py$_3$]$^{2+}$**, which shows even smaller distortion both in XRD [53]

and in DFT. In agreement with the strongly favored **ls** character of both compounds (^{1}H-NMR, UV-Vis, and DFT), direct structural information on the elusive **hs** states was not available in both cases. The analogous zinc(II) complexes **[ZnL]$^{2+}$** (this work) and **[Zn(tren)py$_3$]$^{2+}$** (from [53]), taken as real-world surrogates of the elusive **hs**-species, reveal substantial structural differences that indicate a major structure steering effect of the ligand. In particular, besides elongated metal–nitrogen bond lengths, **[Zn(tren)py$_3$]$^{2+}$** mostly echoes the metrics of **[Fe(tren)py$_3$]$^{2+}$**. This view is fully confirmed by computed structures of **hs-[Fe(tren)py$_3$]$^{2+}$**, optimized with DFT methods on several levels of theory. In consequence, SCO in **[Fe(tren)py$_3$]$^{2+}$** may be termed "structure-conservative", in that an overall octahedral coordination prevails in both spin states. Strikingly, this is not the case in **[FeL]$^{2+}$**, where SCO induces quite severe molecular rearrangements in addition to Fe–N breathing. This conclusion inevitably arises both from the experimental structure of **[ZnL]$^{2+}$** and from the DFT-derived structural data of **hs-[FeL]$^{2+}$**, which give consistent results. In particular, the spin transition induces significant torsional motion within the coordination sphere along the Fe–P–S direction, so that both the zinc(II) complex and the optimized **hs-[FeL]$^{2+}$** structures are no longer adequately described as being octahedral. Overall, SCO in **[FeL]$^{2+}$** cannot be termed "structure-conservative", as the **hs** structure rather approaches a trigonal prismatic structure. As a matter of fact, essentially prismatic coordination of **hs**-iron(II) has been recently reported by us to hold for **[FeL']**(BF$_4$)$_2$ and a closely related complex. We thus conclude that SCO in **[FeL]$^{2+}$** likewise shuttles between an octahedral **ls** state and a trigonal prismatic **hs** state.
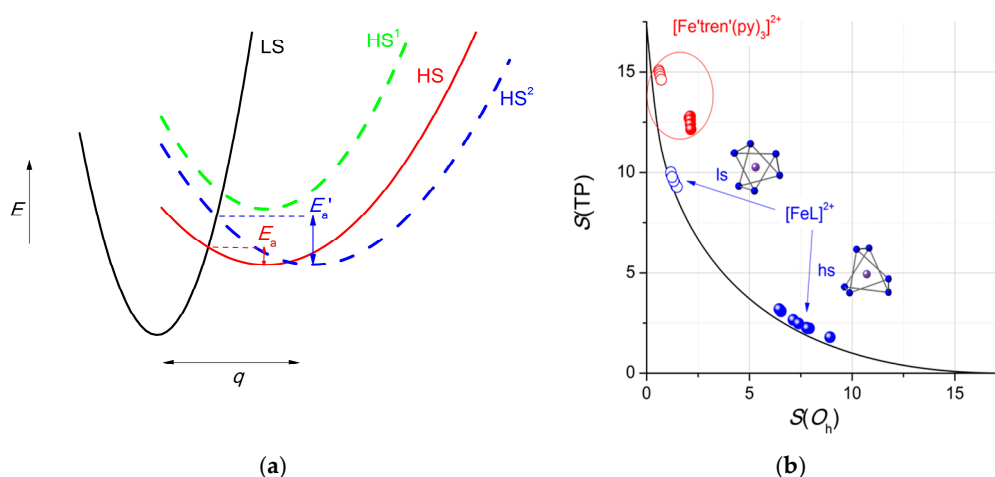
Figure 7. (**a**) Parabolic representation of the potential surface of an SCO complex; effects of vertical (green; variation of $\Delta_{SCO}E$) and horizontal displacements (blue; variation of q) are highlighted; arrows denote the activation barriers.; (**b**) shape map of the O_h–TP structure transition in **[FeL]$^{2+}$** (blue) and **[Zn(tren)py$_3$]$^{2+}$** (red); line: ideal Bailar-type trigonal twist.

Analysis of the structural changes of SCO in terms of the continuous shape measures of Avnir and Alvarez further accentuates the distinctly different influence of the ligand. While the (computed) **ls** and the **hs** state structures of **[Fe(tren)py$_3$]$^{2+}$** give close-lying features on the O_h–TP shape map (red in Figure 7b), a much larger area of the map is covered by the **ls** and the **hs** state structures of **[FeL]$^{2+}$** (blue in Figure 7b). Furthermore, both the **ls** and the **hs** state structures of **[FeL]$^{2+}$** match the implications of Bailar's trigonal twist pathway (line in Figure 7b; [28]). SCO in **[FeL]$^{2+}$** along the Bailar twist is thus highly probable. Additional XRD and DFT work is currently under way to validate this conclusion.

Once having the structural details of SCO in both compounds clarified, the question naturally arises, whether or not the modulated reaction coordinate in **[FeL]$^{2+}$** gives rise to decelerated SCO dynamics. Corresponding results from time-resolved laser spectroscopy and VT-NMR spectroscopy leave no doubt that this is actually the case. The bleach recovery curves of transient absorption

recorded after Vis excitation reveal decay rate constants for **[Fe(tren)py$_3$]$^{2+}$** and **[FeL]$^{2+}$**, which differ by more than one order of magnitude at room temperature, but tend to deviate even more strongly as the temperature is reduced. In consequence, the thermal barrier of SCO in **[FeL]$^{2+}$** is almost doubled with respect to **[Fe(tren)py$_3$]$^{2+}$**. Consistent with the LFP results, dynamic line broadening of the NMR resonances is much more expressed for **[FeL]$^{2+}$**. In agreement with the structural argumentation outlined above, we associate the qualitatively different thermal barriers with qualitatively modulated reaction coordinates. In contrast with this conclusion, we rule out the trivial effects of SCO driving force on the reaction barriers (green in Figure 7a). As DFT-derived SCO energies and thermal drifts of the resonances in the NMR spectra have shown, **[Fe(tren)py$_3$]$^{2+}$** and **[FeL]$^{2+}$** share very similar SCO energies.

4. Materials and Methods

4.1. Computational Methods

All DFT calculations were performed using ORCA2.9.1 [70]. Large TZVPP basis sets [71] were used throughout. The functional scan covers GGA type functionals (PBE [72], BP86 [73]), meta-GGA type functionals (TPSS [74]), hybrid functional (TPSSh [75], B3LYP [76,77]) and four derivatives of B3LYP (20% exact exchange a_0) with reduced exact exchange ($0.00 < a_0 < 0.15$). The structures of **[FeL]$^{2+}$** and of the well-established **[Fe(tren)py$_3$]$^{2+}$** were optimized in their **ls** and **hs** states using each functional. The structures of the respective zinc(II) complexes **[ZnL]$^{2+}$** and **[Zn(tren)py$_3$]$^{2+}$** were optimized with BP86 and B3LYP* ($a_0 = 0.15$). Cartesian coordinates of the B3LYP*-optimized structures of all complexes are given in Tables S4–S9 in the ESI. Apparent SCO energies ($\Delta_{SCO}E = E(\mathbf{hs}) - E(\mathbf{ls})$; negative and positive values of $\Delta_{SCO}E$ denote **hs** and **ls** states, respectively) were derived within the B3LYP family of functionals through application of Jakubikova's concept [57] and referenced to the experimentally known systems **[FeL′]**(BF$_4$)$_2$ [27] and **[Fe(tren)imid$_3$]**(BF$_4$)$_2$ [44–48]. The SCF energies were converged to 10^{-7} Hartree in energy. Dispersion contributions were approximated using Grimme's DFT-D6 atom-pairwise dispersion corrections [78]. Within the B3LYP derivatives dispersion was approximated with the parent B3LYP functional's parameters. Numerical frequency calculations of the BP86-derived structures revealed the stationary points to be minima on the potential surface.

4.2. Materials and General Techniques

All manipulations were performed under an argon atmosphere using standard Schlenk techniques. Diethyl ether was distilled from sodium–potassium alloy/benzophenone and acetonitrile from CaH$_2$ prior to use. CD$_3$CN was vacuum transferred from CaH into thoroughly dried glassware equipped with Young Teflon valves. (S)P(N^{Me}NCHPy)$_3$, was synthesized according to literature procedures [30]. All other chemicals were purchased from Aldrich (Schnelldorf, Germany,) or ABCR (Karlsruhe, Germany,) and were used as received.

4.3. Instrumentation

Elemental analyses and mass spectrometric investigations were carried out in the institutional technical laboratories. UV/Vis spectra in solution were measured using a Varian Cary 50 spectrometer (Varian, Darmstadt, Germany) equipped with a UV/Vis quartz immersion probe (light path 1 mm, Hellma), in a home-built measuring cell. LFP experiments were performed with the 532 nm output of a Nd:YAG laser system [79]. Transient decays were recorded at individual wavelengths by the step-scan method in the range of 320 to 700 nm and obtained as the mean signal of eight pulses. Spectral resolution was in the range of ±5 nm. The duration of the pulses (*fwhm* ca. 8 ns; 2–3 mJ per pulse) was generally much shorter than the decay lifetimes of the transient signals, so that deconvolution was not required for kinetic analysis. Solutions of **[FeL]**(BF$_4$)$_2$ and **[Fe(tren)py$_3$]**(ClO$_4$)$_2$ in high-purity methanol or MeCN (conc.(Fe) $\approx 1 \times 10^{-3}$ M) were rigorously deoxygenated by flushing with analytical grade argon for 20 min prior to and kept under argon during measurement in sealed

quartz cuvettes. For data acquisition at variable temperatures we used a temperature-controlled cell holder (Quantum Northwest, model TC 125). IR spectra were measured using the ATR technique (attenuated total reflection) on a Thermo Nicolet iS5 FT-IR spectrometer (Thermo Fisher Scientific, Berlin, Germany) in the range from 4000 cm^{-1} to 400 cm^{-1}. Solution NMR spectra were recorded with Bruker Avance instruments (Bruker, Rheinstetten, Germany) operating at ^{1}H Larmor frequencies of 200, 400 and 500 MHz and are referenced according to IUPAC recommendations [80]. Chemical shifts are given relative to TMS for ^{13}C and ^{1}H, and H_3PO_4 for ^{31}P. Proton spin–spin coupling patterns in the ^{1}H-NMR spectra of **[FeL](BF$_4$)$_2$** and **[ZnL](ClO$_4$)$_2$** were simulated in MestReC. Linewidths were measured by fitting to Lorenzian shaped curve in Topshim2.1 package. No corrections for possible H–H coupling were applied. The linewidths are generally susceptible to temperature variations and should be seen as good estimations with ca. 10% uncertainty.

4.4. X-ray Crystal Structure Determination

Crystals suitable for X-ray diffraction were obtained from acetonitrile layered with diethyl ether or by diethyl-ether diffusion into acetonitrile solutions. Data were collected at 150.0(1) K using an "Agilent Xcalibur" diffractometer (Agilent Technologies, Yarnton, Oxfordshire, United Kingdom) equipped with a goniometer in κ geometry, a "Sapphire3" CCD-detector, and a graphite-monochromated "Enhance" Mo *K*α source (λ = 0.71073 Å). Diffraction images were integrated with CRYSALISPRO [81]. An analytical absorption correction using a multifaceted crystal model was performed [82]. The structure was solved with SHELXT-2014 [83] using a dual-space method and refined with SHELXL-2017 [84] against $F_o{}^2$ data using the full-matrix least-squares algorithm. OLEX2 was employed as a front end [85]. All non-hydrogen atoms were refined anisotropically. Hydrogen atoms were located on difference Fourier maps (for the complex cations) or their positions were inferred from neighboring sites (for acetonitrile molecules). They were refined with standard riding models. Structure graphics were produced using MERCURY [86].

In **[ZnL](ClO$_4$)$_2$**, the three separate acetonitrile molecules are disordered over the same center of inversion. They have been modelled as rigid bodies (fragment imported from FragmentDB [87]) using enhanced rigid-bond and ADP-similarity restraints. A tightened isotropy restraint was applied to the otherwise physically meaningless anisotropic displacement parameters (ADPs) of the terminal carbon atoms C42 and C52. The occupancy of all acetonitrile molecules was fixed at 0.5 after checking the number of electrons contained in their volume segment using PLATON/SQUEEZE [88]. In **[FeL](BF$_4$)$_2$**, the tetrafluoroborate ion containing B40 exhibits disorder and was modeled in two discrete positions as regularly tetrahedral using tight 1,2-distance, 1,3-distance, rigid-bond and ADP-similarity restraints. Occupancies refined to 0.649(9)/0.351(9); the average B–F bond length refined to 1.355(6) Å. Additionally, the acetonitrile molecule was found rotationally disordered and was modelled in two discrete positions using tight rigid-bond and ADP-similarity restraints. The occupancies refined to 0.74(2)/0.26(2). Due to problems with the beam stop and reflection overlap, seven and ten ill-measured low-angle reflections had to be excluded at the final stage of the refinement of **[ZnL](ClO$_4$)$_2$** and **[FeL](BF$_4$)$_2$**, respectively. The relevant details of the crystals, data collection, and structure refinement are found in Table 1.

4.5. [FeL](BF$_4$)$_2$: [{(S)P(N^{Me}NPy)$_3$}Fe](BF$_4$)$_2$

The synthesis of the iron(II) complex from a tetrafluoroborate precursor has been described in detail recently [25]. Single crystals suitable for X-ray diffraction were obtained from acetonitrile solutions at 4 °C by isothermal diffusion of diethylether within a few days. Yield: 80%. Elemental analysis: Calc. (%) for $C_{21}H_{24}FeN_9SPB_2F_8 \cdot 0.5$ EtOH: C 36.80, N 17.56, H 3.79, S 4.47, found: C 37.70, N 17.58, H 3.48, S 4.02. ^{1}H-NMR (400 MHz, [D$_3$]MeCN, –32 °C): δ [ppm] = 8.63 (d, ^4J = 2.8 Hz, 3H, H5), 8.15 (m, 6H, H3,4), 7.43 (m, 3H, H2), 6.52 (d, ^3J = 5.6 Hz, 3H, H1) 3.47 (d, ^3J = 12.8 Hz, 9H, N–Me). {^{1}H}^{13}C-NMR (50.32 MHz, [D$_3$]MeCN, 25 °C): δ [ppm] = 156.2 (s, 3C, pyC), 154.7 (s, 3C, pyC), 151.3 (d, ^3J = 8 Hz, 3C, *C*=N$_{ald}$), 140.5 (s, 3C, C_{Ar}), 129.2 (s, 3C, C_{Ar}), 128.1 (s, 3C, C_{Ar}), 38.4 (d, 9C,

^2J = 3 Hz, N–CH_3). {^{1}H}^{31}P-NMR (80.95 MHz, [D$_3$]MeCN, 25 °C): δ [ppm] = 65.5. HR-MS (ESI) Calc. for C$_{21}$H$_{24}$FeN$_9$PS: [M]$^{2+}$ = 260.5473; found: [M]$^{2+}$ 260.5475. IR (KBr): $\tilde{v}$ [cm^{-1}] = 3432bs, 3102w, 3056w, 2923w, 1607s, 1576m, 1466s, 1444m, 1243m, 1161s, 1052s, 952m, 897w, 802s, 572w, 519w.

4.6. [ZnL](ClO$_4$)$_2$: [{(S)P(N^{Me}NPy)$_3$}Zn](ClO$_4$)$_2$

To a stirred solution of (S)P(N^{Me}NCHPy)$_3$ (104 mg, 0.22 mmol) in 4 mL degassed ethanol a solution of [Zn(ClO$_4$)$_2$ × 6 H$_2$O] (83 mg, 0.22 mmol) in 2 mL ethanol was added dropwise at room temperature. After stirring the obtained colorless suspension over night the reaction mixture was filtered and the precipitate washed with 2 × 3 mL diethylether. Colorless crystals suitable for X-ray diffraction were obtained from acetonitrile solutions of the complex salt by isothermal diffusion of diethylether at 4 °C within a few days. Yield: 123 mg (77%). elemental analysis (%) calcd. for C$_{21}$H$_{24}$N$_9$O$_6$PSZnCl$_2$O$_8$: C 34.56, H 3.31, N 17.27, S 4.39; found: C 34.36, H 3.28, N 17.23, S 4.06; ^{1}H-NMR (200 MHz, 298 K, [D$_3$]MeCN): δ = 3.53 (d, $^3J_{HP}$ = 10.8 Hz, 9H, N–CH_3), 7.72 (ddd, $^3J_{HH}$ = 7.8 Hz, $^3J_{HH}$ = 5.0 Hz, $^4J_{HH}$ = 1.5 Hz, 3H, H^2), 7.87 (ddd, $^3J_{HH}$ = 7.8 Hz, $^4J_{HH}$ = 1.5 Hz, $^5J_{HH}$ = 0.8 Hz, 3H, H^4), 8.12 (ddd, $^3J_{HH}$ = 5.0 Hz, $^4J_{HH}$ = 1.6 Hz, $^5J_{HH}$ = 0.8 Hz, 3H, H^1), 8.18 (s (br), 3H, H^5), 8.26 (dt, $^3J_{HH}$ = 7.8 Hz, $^4J_{HH}$ = 1.6 Hz, 3H, H^3) ppm; ^{13}C{^{1}H}-NMR (50.32 MHz, 298 K, [D$_3$]MeCN): δ = 35.3 (d, $^2J_{CP}$ = 10.0 Hz, N–CH_3), 127.1 (s, 3C, C_{Ar}), 127.8 (s, 3C, C_{Ar}), 139.8 (d, $^3J_{CP}$ = 9.0 Hz, C=N$_{ald}$), 142.7 (s, 3C, C_{Ar}), 148.1 (s, 3C, C_{Ar}), 148.8 (s, 3C, C_{Ar}) ppm; ^{31}P{^{1}H}-NMR (80.95 MHz, 298 K, [D$_3$]MeCN): δ = 56.2 (s) ppm.

Author Contributions: Gerald Hörner conceived and designed the experiments; Philipp Stock, Gerald Hörner and Holm Petzold performed the experiments; Holm Petzold and Gerald Hörner analyzed the data; Dennis Wiedemann contributed crystallographic work; Gerald Hörner wrote the paper.

Conflicts of Interest: The authors declare no conflict of interest.

References

1. Halcrow, M.A. (Ed.) *Spin Crossover Materials*; Wiley: Chichester, UK, 2013.

2. Kahn, O.; Martinez, C.J. Spin-Transition Polymers: From Molecular Materials toward Memory Devices. *Science* **1998**, *279*, 44–48. [CrossRef]

3. Létard, J.-F.; Guionneau, P.; Gouz-Capes, L. Towards Spin Crossover Applications. *Top. Curr. Chem.* **2004**, *235*, 221–249. [CrossRef]

4. Gütlich, P.; Gaspar, A.B.; Garcia, Y. Spin state switching in iron coordination compounds. *Beilstein J. Org. Chem.* **2013**, *9*, 342–391. [CrossRef] [PubMed]

5. Bousseksou, A.; Molnar, G.; Salmon, L.; Nicolazzi, W. Molecular spin crossover phenomenon: Recent achievements and prospects. *Chem. Soc. Rev.* **2011**, *40*, 3313–3335. [CrossRef] [PubMed]

6. Sato, O.; Tao, J.; Zhang, Y.-Z. Controlling Magnetic Properties through External Stimuli. *Angew. Chem. Int. Ed.* **2006**, *46*, 2152. [CrossRef] [PubMed]

7. Kumar, K.S.; Ruben, M. Emerging trends in spin crossover (SCO) based functional materials and devices. *Coord. Chem. Rev.* **2017**, *346*, 176–205. [CrossRef]

8. Decurtins, S.; Gütlich, P.; Köhler, C.P.; Spiering, H.; Hauser, A. Light-induced excited spin state trapping in a transition-metal complex: The hexa-1-propyltetrazole-iron (II) tetrafluoroborate spin-crossover system. *Chem. Phys. Lett.* **1984**, *105*, 1–4. [CrossRef]

9. Letard, J.-F.; Asthana, S.; Shepherd, H.J.; Guionneau, P.; Goeta, A.E.; Suemura, N.; Ishikawa, R.; Kaizaki, S. Photomagnetism of a sym-*cis*-Dithiocyanato Iron(II) Complex with a Tetradentate *N*,*N'*-Bis(2-pyridylmethyl)1,2-ethanediamine Ligand. *Chem. Eur. J.* **2012**, *19*, 5924–5934. [CrossRef] [PubMed]

10. Letard, J.-F.; Capes, L.; Chastanet, G.; Molinar, N.; Letard, S.; Real, J.-A.; Kahn, O. Critical temperature of the LIESST effect in iron(II) spin crossover compounds. *Chem. Phys. Lett.* **1999**, *313*, 115–120. [CrossRef]

11. Hauser, A.; Enachescu, C.; Daku, M.L.; Vargas, A.; Amstutz, N. Low-temperature lifetimes of metastable high-spin states in spin-crossover and in low-spin iron(II) compounds: The rule and exceptions to the rule. *Coord. Chem. Rev.* **2006**, *250*, 1642–1652. [CrossRef]

12. Klingele, J.; Kaase, D.; Schmucker, M.; Lan, Y.H.; Chastanet, G.; Letard, J.-F. Thermal Spin Crossover and LIESST Effect Observed in Complexes [Fe(LCh)$_2$(NCX)$_2$] [LCh = 2,5-Di(2-Pyridyl)-1,3,4-Chalcadiazole; Ch = O, S, Se; X = S, Se, BH$_3$]. *Inorg. Chem.* **2013**, *52*, 6000–6010. [CrossRef] [PubMed]

13. Dose, E.V.; Hoselton, M.A.; Sutin, N.; Tweedle, M.F.; Wilson, L.J. Dynamics of intersystem crossing processes in solution for six-coordinate d5, d6, and d7 spin-equilibrium metal complexes of iron(III), iron(II), and cobalt(II). *J. Am. Chem. Soc.* **1978**, *100*, 1141–1147. [CrossRef]

14. Garvey, J.J.; Lawthers, I. Photochemically-induced perturbation of the 1A ⇌ 5T equilibrium in FeII complexes by pulsed laser irradiation in the metal-to-ligand charge-transfer absorption band. *J. Chem. Soc. Chem. Commun.* **1982**, 906–907. [CrossRef]

15. Beattie, J.K. Dynamics of Spin Equilibria in Metal Complexes. *Adv. Inorg. Chem.* **1988**, *32*, 1–53. [CrossRef]

16. Toftlund, H. Spin equilibria in iron(II) complexes. *Coord. Chem. Rev.* **1989**, *94*, 67–108. [CrossRef]

17. Xie, C.-L.; Hendrickson, D.N. Mechanism of spin-state interconversion in ferrous spin-crossover complexes: Direct evidence for quantum mechanical tunneling. *J. Am. Chem. Soc.* **1987**, *109*, 6981–6988. [CrossRef]

18. Al-Obaidi, A.H.R.; Jensen, K.B.; McGarvey, J.J.; Toftlund, H.; Jensen, B.; Bell, S.E.J.; Carroll, J.G. Structural and Kinetic Studies of Spin Crossover in an Iron(II) Complex with a Novel Tripodal Ligand. *Inorg. Chem.* **1996**, *35*, 5055–5060. [CrossRef] [PubMed]

19. Chang, H.-R.; McCusker, J.K.; Toftlund, H.; Wilson, S.R.; Trautwein, A.X.; Winkler, H.; Hendrickson, D.N. [Tetrakis(2-pyridylmethyl)ethylenediamine]iron(II) perchlorate, the first rapidly interconverting ferrous spin-crossover complex. *J. Am. Chem. Soc.* **1990**, *112*, 6814–6827. [CrossRef]

20. McCusker, J.K.; Toftlund, H.; Rheingold, A.L.; Hendrickson, D.N. Ligand conformational changes affecting 5T2 → 1A1 intersystem crossing in a ferrous complex. *J. Am. Chem. Soc.* **1993**, *115*, 1797–1804. [CrossRef]

21. Brady, C.; McGarvey, J.J.; McCusker, J.K.; Toftlund, H.; Hendrickson, D.N. Time-Resolved Relaxation Studies of Spin Crossover Systems in Solution. *Top. Curr. Chem.* **2004**, *235*, 1–22. [CrossRef]

22. McCusker, J.K.; Rheingold, A.L.; Hendrickson, D.N. Variable-Temperature Studies of Laser-Initiated 5T2 → 1A1 Intersystem Crossing in Spin-Crossover Complexes: Empirical Correlations between Activation Parameters and Ligand Structure in a Series of Polypyridyl Ferrous Complexes. *Inorg. Chem.* **1996**, *35*, 2100–2112. [CrossRef]

23. Hain, S.K.; Heinemann, F.W.; Gieb, K.; Müller, P.; Hörner, G.; Grohmann, A. On the Spin Behaviour of Iron(II)–Dipyridyltriazine Complexes and Their Performance as Thermal and Photonic Spin Switches. *Eur. J. Inorg. Chem.* **2010**, 221–232. [CrossRef]

24. Fatur, S.M.; Shepard, S.G.; Higgins, R.F.; Shores, M.P.; Damrauer, N.H. A Synthetically Tunable System To Control MLCT Excited-State Lifetimes and Spin States in Iron(II) Polypyridines. *J. Am. Chem. Soc.* **2017**, *139*, 4493–4505. [CrossRef] [PubMed]

25. Stock, P.; Pędziński, T.; Spintig, N.; Grohmann, A.; Hörner, G. High Intrinsic Barriers against Spin-State Relaxation in Iron(II)-Complex Solutions. *Chem. Eur. J.* **2013**, *19*, 839–842. [CrossRef] [PubMed]

26. Stock, P.; Spintig, N.; Scholz, J.; Epping, J.D.; Oelsner, C.; Wiedemann, D.; Grohmann, A.; Hörner, G. Spin-State Dynamics of a Photochromic Iron(II) Complex and its Immobilization on Oxide Surfaces Via Phenol Anchors. *J. Coord. Chem.* **2015**, *68*, 3099–3115. [CrossRef]

27. Stock, P.; Deck, E.; Hohnstein, S.; Korzekwa, J.; Meyer, K.; Heinemann, F.W.; Breher, F.; Hörner, G. Molecular Spin Crossover in Slow Motion: Light-Induced Spin-State Transitions in Trigonal Prismatic Iron(II) Complexes. *Inorg. Chem.* **2016**, *55*, 5254–5265. [CrossRef] [PubMed]

28. Bailar, J.C., Jr. Some problems in the stereochemistry of coordination compounds: Introductory lecture. *J. Inorg. Nucl. Chem.* **1958**, *8*, 165–175. [CrossRef]

29. Trapp, I.; Löble, M.W.; Meyer, J.; Breher, F. Copper complexes of tripodal $\kappa^6 N$-donor ligands: A structural, EPR spectroscopic and electrochemical study. *Inorg. Chim. Acta* **2011**, *374*, 373–384. [CrossRef]

30. Löble, M.W.; Casimiro, M.; Thielemann, D.T.; Oña-Burgos, P.; Fernandez, I.; Roesky, P.W.; Breher, F. 1H,89Y HMQC and Further NMR Spectroscopic and X-ray Diffraction Investigations on Yttrium-Containing Complexes Exhibiting Various Nuclearities. *Chem. Eur. J.* **2012**, *18*, 5325–5334. [CrossRef] [PubMed]

31. Chandrasekhar, V.; Azhakar, R.; Pandian, B.M.; Boomishankar, R.; Steiner, A. A phosphorus-supported multisite coordination ligand containing three imidazolyl arms and its metalation behaviour. An unprecedented co-existence of mononuclear and macrocyclic dinuclear Zn(II) complexes in the same unit cell of a crystalline lattice. *Dalton Trans.* **2008**, *37*, 5962–5969. [CrossRef] [PubMed]

32. Marchivie, M.; Guionneau, P.; Letard, J.-F.; Chasseau, D. Photo-induced spin-transition: The role of the iron(II) environment distortion. *Acta Crystallogr. Sect. B Struct. Sci.* **2005**, *61*, 25–28. [CrossRef] [PubMed]

33. Fleischer, E.B.; Gebala, A.E.; Swift, D.R.; Tasker, P.A. Trigonal prismatic-octahedral coordination. Complexes of intermediate geometry. *Inorg. Chem.* **1972**, *11*, 2775–2784. [CrossRef]

34. Wentworth, R.A.D. Trigonal prismatic vs. octahedral stereochemistry in complexes derived from innocent ligands. *Coord. Chem. Rev.* **1972**, *9*, 171–187. [CrossRef]

35. Purcell, K.F. Pseudorotational intersystem crossing in d6 complexes. *J. Am. Chem. Soc.* **1979**, *101*, 5147–5152. [CrossRef]

36. Vanquickenborne, L.G.; Pierloot, K. Role of spin change in the stereomobile reactions of strong-field d6 transition-metal complexes. *Inorg. Chem.* **1981**, *20*, 3673–3677. [CrossRef]

37. Comba, P. Coordination geometries of hexaamine cage complexes. *Inorg. Chem.* **1989**, *28*, 426–431. [CrossRef]

38. Larsen, E.; La Mar, G.N.; Wagner, B.E.; Parks, J.E.; Holm, R.H. Three-dimensional macrocyclic encapsulation reactions. III. Geometrical and electronic features of tris(diimine) complexes of trigonal-prismatic, antiprismatic, and intermediate stereochemistry. *Inorg. Chem.* **1972**, *11*, 2652–2668. [CrossRef]

39. Comba, P.; Sargeson, A.M.; Engelhardt, L.M.; Harrowfield, J.M.B.; White, A.H.; Horn, E.; Snow, M.R. Analysis of trigonal-prismatic and octahedral preferences in hexaamine cage complexes. *Inorg. Chem.* **1985**, *24*, 2325–2327. [CrossRef]

40. Alvarez, S.; Avnir, D.; Llunell, M.; Pinsky, M. Continuous symmetry maps and shape classification. The case of six-coordinated metal compounds. *New J. Chem.* **2002**, *26*, 996–1009. [CrossRef]

41. Knight, J.C.; Alvarez, S.; Amoroso, A.J.; Edwards, P.G.; Singh, N. A novel bipyridine-based hexadentate tripodal framework with a strong preference for trigonal prismatic co-ordination geometries. *Dalton Trans.* **2010**, *39*, 3870–3883. [CrossRef] [PubMed]

42. Alvarez, S. Distortion Pathways of Transition Metal Coordination Polyhedra Induced by Chelating Topology. *Chem. Rev.* **2015**, *115*, 13447–13483. [CrossRef] [PubMed]

43. Conti, A.J.; Xie, C.L.; Hendrickson, D.N. Tunneling in spin-state interconversion of ferrous spin-crossover complexes. Concentration dependence of apparent activation energy determined in solution by laser-flash photolysis. *J. Am. Chem. Soc.* **1989**, *111*, 1171–1180. [CrossRef]

44. Brewer, G.; Olida, M.J.; Schmiedekamp, A.M.; Viragh, C.; Zavalij, P.Y. A DFT computational study of spin crossover in iron(III) and iron(II) tripodal imidazole complexes. A comparison of experiment with calculations. *Dalton Trans.* **2006**, *35*, 5617. [CrossRef] [PubMed]

45. Sunatsuki, Y.; Ikuta, Y.; Matsumoto, N.; Ohta, H.; Kojima, M.; Iijima, S.; Hayami, S.; Maeda, Y.; Kaizaki, S.; Dahan, F.; Tuchagues, J.-P. An Unprecedented Homochiral Mixed-Valence Spin-Crossover Compound. *Angew. Chem. Int. Ed.* **2003**, *42*, 1614. [CrossRef] [PubMed]

46. Ohta, H.; Sunatsuki, Y.; Kojima, M.; Iijima, S.; Akashi, H.; Matsumoto, N. A Tripodal Ligand Containing Three Imidazole Groups Inducing Spin Crossover in Both Fe(II) and Fe(III) Complexes; Structures and Spin Crossover Behaviors of the Complexes. *Chem. Lett.* **2004**, *33*, 350. [CrossRef]

47. Sunatsuki, Y.; Ohta, H.; Kojima, M.; Ikuta, Y.; Goto, Y.; Matsumoto, N.; Iijima, S.; Akashi, H.; Kaizaki, S.; Dahan, F.; et al. Supramolecular Spin-Crossover Iron Complexes Based on Imidazole-Imidazolate Hydrogen Bonds. *Inorg. Chem.* **2004**, *43*, 4154. [CrossRef] [PubMed]

48. Brewer, C.; Brewer, G.; Luckett, C.; Marbury, G.S.; Viragh, C.; Beatty, A.M.; Scheidt, W.R. Proton Control of Oxidation and Spin State in a Series of Iron Tripodal Imidazole Complexes. *Inorg. Chem.* **2004**, *43*, 2402. [CrossRef] [PubMed]

49. Halcrow, M.A. Structure: Function relationships in molecular spin-crossover complexes. *Chem. Soc. Rev.* **2011**, *40*, 4119–4142. [CrossRef] [PubMed]

50. Weber, B.; Bauer, W.; Obel, J. An Iron(II) Spin-Crossover Complex with a 70 K Wide Thermal Hysteresis Loop. *Angew. Chem Int. Ed.* **2008**, *47*, 10098–10101. [CrossRef] [PubMed]

51. Stock, P.; Erbe, A.; Buck, M.; Wiedemann, D.; Menard, H.; Hörner, G.; Grohmann, A. Thiocyanate Anchors for Salt-like Iron(II) Complexes on Au(111): Promises and Caveats. *Z. Naturforsch. B A J. Chem. Sci.* **2014**, *69*, 1164–1180. [CrossRef]

52. Hostettler, M.; Törnroos, K.W.; Chernyshow, D.; Vangdal, B.; Bürgi, H.-B. Challenges in Engineering Spin Crossover: Structures and Magnetic Properties of Six Alcohol Solvates of Iron(II) Tris(2-picolylamine) Dichloride. *Angew. Chem. Int. Ed.* **2004**, *43*, 4589–4594. [CrossRef] [PubMed]

53. Kirchner, R.M.; Mealli, C.; Bailey, M.; Howe, N.; Torre, L.P.; Wilson, L.J.; Andrews, L.C.; Rose, N.J.; Lingafelter, E.C. The Variable Coordination Chemistry of a Potentially Heptadentate Ligand with a Series of 3d Transition Metal Ions. The Chemistry and the Strcutures of [M(py3tren)]$^{2+}$, where M(II) = Mn, Fe, Co, Ni, Cu and Zn and (py3tren) = N{CH$_2$CH$_2$N=C(H)(C$_5$H$_4$N)}$_3$. *Coord. Chem. Rev.* **1987**, *77*, 89–163. [CrossRef]

54. Lazar, H.Z.; Forestier, T.; Barrett, S.A.; Kilner, C.A.; Letard, J.-F.; Halcrow, M.A. Thermal and light-induced spin-crossover in salts of the heptadentate complex [tris(4-{pyrazol-3-yl}-3-aza-3-butenyl)amine]iron(II). *Dalton Trans.* **2007**, *36*, 4276–4285. [CrossRef] [PubMed]

55. Reiher, M.; Salomon, O.; Hess, B.A. Reparameterization of hybrid functionals based on energy differences of states of different multiplicity. *Theor. Chem. Acc.* **2001**, *107*, 48–55. [CrossRef]

56. Lawson Daku, M.L.; Vargas, A.; Hauser, A.; Fouqueau, A.; Casida, M.E. Assessment of Density Functionals for the High-Spin/Low-Spin Energy Difference in the Low-Spin Iron(II) Tris(2,2'-bipyridine) Complex. *ChemPhysChem* **2005**, *6*, 1393–1410. [CrossRef] [PubMed]

57. Bowman, D.N.; Jakubikova, E. Low-Spin versus High-Spin Ground State in Pseudo-Octahedral Iron Complexes. *Inorg. Chem.* **2012**, *51*, 6011–6019. [CrossRef] [PubMed]

58. Bowman, D.N.; Bondarev, A.; Mukherjee, S.; Jakubikova, E. Tuning the Electronic Structure of Fe(II) Polypyridines via Donor Atom and Ligand Scaffold Modifications: A Computational Study. *Inorg. Chem.* **2015**, *54*, 8786–8793. [CrossRef] [PubMed]

59. Mengel, A.K.C.; Förster, C.; Breivogel, A.; Mack, K.; Ochsmann, J.R.; Laquai, F.; Ksenofontov, V.; Heinze, K. Heteroleptic Push-Pull Substituted Iron(II) Bis(tridentate) Complex with Low Energy Charge Transfer States. *Chem. Eur. J.* **2015**, *21*, 704–714. [CrossRef] [PubMed]

60. Jamula, L.L.; Brown, A.M.; Guo, D.; McCusker, J.K. Synthesis and characterization of a high-symmetry ferrous polypyridyl complex: Approaching the $^5T_2/^3T_1$ crossing point for Fe^{II}. *Inorg. Chem.* **2014**, *53*, 15–17. [CrossRef] [PubMed]

61. Buhks, E.; Navon, G.; Bixon, M.; Jortner, J. Spin Conversion Processes in Solutions. *J. Am. Chem. Soc.* **1980**, *102*, 2918–2923. [CrossRef]

62. Barrett, S.A.; Kilner, C.A.; Halcrow, M.A. Spin-crossover in [Fe(3-bpp)$_2$][BF$_4$]$_2$ in different solvents—A dramatic stabilisation of the low-spin state in water. *Dalton Trans.* **2011**, *40*, 12021–12024. [CrossRef] [PubMed]

63. Petzold, H.; Djomgoue, P.; Hörner, G.; Speck, J.M.; Rüffer, T.; Schaarschmidt, D. 1H-NMR spectroscopic elucidation in solution of the kinetics and thermodynamics of spin crossover for an exceptionally robust Fe^{2+} complex. *Dalton Trans.* **2016**, *45*, 13798–13809. [CrossRef] [PubMed]

64. Petzold, H.; Djomgoue, P.; Hörner, G.; Heider, S.; Lochenie, C.; Weber, B.; Rüffer, T.; Schaarschmidt, D. Spin state variability in Fe^{2+} complexes of substituted (2-(pyridin-2-yl)-1,10-phenanthroline) ligands as versatile terpyridine analogues. *Dalton Trans.* **2017**, *46*, 6218–6229. [CrossRef] [PubMed]

65. Petzold, H.; Djomgoue, P.; Hörner, G.; Lochenie, C.; Weber, B.; Rüffer, T. Bis-meridional Fe^{2+} SCO complexes of phenyl and pyridyl substituted 2-(pyridin-2-yl)-1,10-phenanthrolines. *Dalton Trans.* **2017**. (under Review).

66. Renz, F.; Oshio, H.; Ksenofontov, V.; Waldeck, M.; Spiering, H.; Gütlich, P. Strong Field Iron(II) Complex Converted by Light into a Long-Lived High-Spin State. *Angew. Chem. Int. Ed.* **2000**, *39*, 3699–3700. [CrossRef]

67. Vanko, G.; Bordage, A.; Papai, M.; Haldrup, K.; Glatzel, P.; March, A.M.; Doumy, G.; Britz, A.; Galler, A.; Assefa, T.; et al. Detailed Characterization of a Nanosecond-Lived Excited State: X-ray and Theoretical Investigation of the Quintet State in Photoexcited $[Fe(terpy)_2]^{2+}$. *J. Phys. Chem. C* **2015**, *119*, 5888–5902. [CrossRef] [PubMed]

68. Zhang, X.; Lawson Daku, M.L.; Zhang, J.; Suarez-Alcantara, K.; Jennings, G.; Kurtz, C.A.; Canton, S.E. Dynamic Jahn–Teller Effect in the Metastable High-Spin State of Solvated $[Fe(terpy)_2]^{2+}$. *J. Phys. Chem. C* **2015**, *119*, 3312–3321. [CrossRef]

69. Canton, S.E.; Zhang, X.; Lawson Daku, M.L.; Liu, Y.; Zhang, J.; Alvarez, S. Mapping the Ultrafast Changes of Continuous Shape Measures in Photoexcited Spin Crossover Complexes without Long-Range Order. *J. Phys. Chem. C* **2015**, *119*, 3322–3330. [CrossRef]

70. Neese, F. The ORCA program system. *WIREs Comput. Mol. Sci.* **2012**, *2*, 73–78. [CrossRef]

71. Schäfer, A.; Horn, H.; Ahlrichs, R. Fully optimized contracted Gaussian basis sets for atoms Li to Kr. *J. Chem. Phys.* **1992**, *97*, 2571–2577. [CrossRef]

72. Perdew, J.P.; Burke, K.; Ernzerhof, M. Generalized Gradient Approximation Made Simple. *Phys. Rev. Lett.* **1996**, *77*, 3865–3868. [CrossRef] [PubMed]

73. Becke, A.D. Density-functional exchange-energy approximation with correct asymptotic behavior. *Phys. Rev. A* **1988**, *38*, 3098–3100. [CrossRef]

74. Kanai, Y.; Wang, X.; Selloni, A.; Car, R. Testing the TPSS meta-generalized-gradient-approximation exchange-correlation functional in calculations of transition states and reaction barriers. *J. Chem. Phys.* **2006**, *125*, 234104. [CrossRef] [PubMed]

75. Staroverov, V.N.; Scuseria, G.E.; Tao, J.; Perdew, J.P. Comparative assessment of a new nonempirical density functional: Molecules and hydrogen-bonded complexes. *J. Chem. Phys.* **2003**, *119*, 12129. [CrossRef]

76. Becke, A.D. Density-functional thermochemistry. III. The role of exact exchange. *J. Chem. Phys.* **1993**, *98*, 5648–5652. [CrossRef]

77. Lee, C.; Yang, W.; Parr, R.G. Development of the Colle-Salvetti correlation-energy formula into a functional of the electron density. *Phys. Rev. B* **1988**, *37*, 785–789. [CrossRef]

78. Grimme, S. Semiempirical GGA-type density functional constructed with a long-range dispersion correction. *J. Comput. Chem.* **2006**, *27*, 1787–1799. [CrossRef] [PubMed]

79. Pędziński, T.; Markiewicz, A.; Marciniak, B. Photosensitized oxidation of methionine derivatives. Laser flash photolysis studies. *Res. Chem. Intermed.* **2009**, *35*, 497–506. [CrossRef]

80. Harris, R.K.; Becker, E.D.; Cabral de Menezes, S.M.; Granger, P.; Hoffman, R.E.; Zilm, K.W. Further conventions for NMR shielding and chemical shifts. *Pure Appl. Chem.* **2008**, *80*, 59–84. [CrossRef]

81. *CrysAlisPro Software System*, version 1.171.37. Intelligent Data Collection and Processing Software for Small Molecule and Protein Crystallography. Agilent Technologies: Oxford, UK, 2014.

82. Clark, R.C.; Reid, J.S. The analytical calculation of absorption in multifaceted crystals. *Acta Crystallogr. Sect. A Found. Crystallogr.* **1995**, *51*, 887–897. [CrossRef]

83. Sheldrick, G. *SHELXT*—Integrated space-group and crystal-structure determination. *Acta Crystallogr. Sect. A Found. Adv.* **2015**, *71*, 3–8. [CrossRef] [PubMed]

84. Sheldrick, G. Crystal structure refinement with *SHELXL. Acta Crystallogr. Sect. C Struct. Chem.* **2015**, *71*, 3–8. [CrossRef] [PubMed]

85. Dolomanov, O.V.; Bourhis, L.J.; Gildea, R.J.; Howard, J.A.K.; Puschmann, H. OLEX2: A complete structure solution, refinement and analysis program. *J. Appl. Crystallogr.* **2009**, *42*, 339–341. [CrossRef]

86. Macrae, C.F.; Bruno, I.J.; Chisholm, J.A.; Edgington, P.R.; McCabe, P.; Pidcock, E.; Rodriguez-Monge, L.; Taylor, R.; van de Streek, J.; Wood, P.A. Mercury CSD 2.0—New features for the visualization and investigation of crystal structures. *J. Appl. Crystallogr.* **2008**, *41*, 466–470. [CrossRef]

87. Kratzert, D.; Holstein, J.J.; Krossing, I. DSR: Enhanced modelling and refinement of disordered structures with *SHELXL. J. Appl. Crystallogr.* **2015**, *48*, 933–938. [CrossRef] [PubMed]

88. Spek, A.L. PLATON SQUEEZE: A tool for the calculation of the disordered solvent contribution to the calculated structure factors. *Acta Crystallogr. Sect. C Struct. Chem.* **2015**, *71*, 9–18. [CrossRef] [PubMed]